RESEARCH ARTICLE | AUGUST 13 2025

Comparative study of regression-based data-driven models for thermally stratified Carreau nanofluids with magnesium oxide nanoparticles

Aamir Farooq ; Sadique Rehman ; Wen-Xiu Ma

Physics of Fluids 37, 082032 (2025)
https://doi.org/10.1063/5.0274063

Physics of Fluids ARTICLE pubs.aip.org/aip/pof

Comparative study of regression-based data-driven models for thermally stratified Carreau nanofluids with magnesium oxide nanoparticles

Cite as: Phys. Fluids **37**, 082032 (2025); doi: 10.1063/5.0274063
Submitted: 3 April 2025 · Accepted: 14 July 2025 ·
Published Online: 13 August 2025

Aamir Farooq,[1] Sadique Rehman,[2,a)] and Wen-Xiu Ma[1,3,4,5,b)]

AFFILIATIONS

[1]Department of Mathematics, Zhejiang Normal University 321004, People's Republic of China
[2]Division of Mathematical and Physical Sciences, Kanazawa University, Kakuma, Kanazawa 920-1192, Japan
[3]Department of Mathematics, King Abdulaziz University, Jeddah 21589, Saudi Arabia
[4]Department of Mathematics and Statistics, University of South Florida, Tampa, Florida 33620-5700, USA
[5]Material Science Innovation and Modelling, North-West University, Mafikeng Campus, Private Bag X2046, Mmabatho 2735, South Africa

[a)]Electronic mail: sadique@stu.kanazawa-u.ac.jp
[b)]Author to whom correspondence should be addressed: mawx@cas.usf.edu

ABSTRACT

This study examines the two-dimensional flow of a Carreau nanofluid over a thin stretching surface, incorporating melting heat effects and considering both thermal and concentration stratification under an inclined magnetic field and multiple slip conditions. Milk is used as the base fluid, with magnesium oxide nanoparticles added to enhance thermal properties and support biomedical cooling and drug delivery applications. The governing momentum, temperature, and concentration equations are transformed into a nonlinear ordinary differential equations system using local similarity variables. These equations are initially solved using the three-stage Lobatto IIIa implicit Runge–Kutta method to generate a reference dataset. Subsequently, a data-driven modeling approach is employed, utilizing an artificial neural network trained with a backpropagation algorithm and Bayesian regularization to ensure solution accuracy and stability. To evaluate the robustness of the network, Gaussian noise of varying intensity is added exclusively to the test data, while the model is trained on clean reference data. The performance is then assessed on both noise-free and noisy test inputs using relative error based on the Euclidean norm. Furthermore, six regression models, linear, ridge, and lasso (linear models), along with decision tree, support vector regression, and Gaussian process regression (nonlinear models), are employed to estimate key engineering parameters, including the Nusselt number, the Sherwood number, and the skin friction coefficient. These predictions are quantitatively verified using the correlation matrices, mean squared error, and coefficient of determination, comprehensively assessing each model's accuracy. This study integrates regression-based techniques with data-driven neural networks to derive heat and mass transfer solutions in stratified nanofluid flow. The proposed methodology offers a robust framework for analyzing nonlinear thermal systems with uncertainties, with promising applications in biomedical and industrial domains.

NOMENCLATURE

A	Ratio parameter
B_0	Strength of magnetic field
C	Concentration
C_m, C_∞	Melting and surrounding concentration
C_f	Skin-friction coefficient
$c_{p,nf}$	Heat capacity
c_s	Solid surface heat capacity
$[d_1, d_2, e_1, e_2]$	Dimensional constants
Ec	Eckert number
f'	Dimensionless velocity
Ha	Magnetic parameter
k', k''	Thermal and solutal slip parameters
K_1	Chemical reaction ratio
k_{nf}	Thermal conductivity

M_0	Melting parameter
Nu	Nusselt number
n	Micro-gyration
nf	Nanofluid
Kr	Chemical reaction parameter
Pr	Prandtl number
p	Pressure
Q^*	Heat source/sink
Sc	Schmidt number
Sc	Schmidt number
s_1, s_2	Thermal and solutal stratification parameters
T	Temperature
T_m, T_∞	Melting and surrounding temperature
u_w	Velocity of stretching sheet
$[u, v]$	Velocity components
We	Weissenberg number
[x, y]	Rectangular coordinates
α	Angle of inclination
ϵ	Latent heat of the fluid
λ	Relaxation time
μ_0, μ_∞	Zero and infinite shear viscosity
ν_{nf}	Kinematic viscosity
ζ	Similarity variable
ρ_{nf}	Density
σ_{nf}	Electrical conductivity
ϕ	Dimensionless concentration
θ	Dimensionless temperature

I. INTRODUCTION

Nanofluids, recognized for their exceptional ability to enhance heat and mass transfer, are pivotal in various engineering domains, including electronics cooling, manufacturing, and biomedical technologies. These fluids, composed of suspended nanoparticles such as metals, oxides, carbides, and carbon nanotubes, significantly improve thermal conductivity and energy efficiency, particularly in heat exchanger systems. Applications extend across microelectronics, fuel cells, medical treatments, and hybrid vehicle engines, owing to their superior heat dissipation capabilities. In the biomedical sector, magnesium nanoparticles have been suspended in milk to combat magnesium deficiencies in children, which can lead to personality changes, muscle spasms, and seizures. Nabwey *et al.*[38] explored the bioconvection effect on MHD Carreau nanofluid flow around an inclined cylinder using MATLAB simulations. Waqas *et al.*[57] analyzed 3D Carreau nanofluid flow involving microorganisms and thermal source/sink terms. Similarly, Ramzan *et al.*[43] investigated bio-convected Williamson ferro-nanofluids with magnetic dipole and activation energy, while Farooq *et al.*[14] examined Maxwell nanofluid vibrations involving coupled heat and mass transport. Wang *et al.*[56] studied a blood-gold-based Oldroyd-B nanofluid in a porous medium under MHD conditions, and Mahdy[35] along with Xia *et al.*[58] analyzed bioconvection and activation energy effects in Powell–Eyring nanofluids.

Ali and Summayya[3] and Abo-Zaid *et al.*[1] contributed to Powell–Eyring nanofluid modeling, while Javed and Farooq[23] focused on mixed convection with melting effects. Gangadhar *et al.*[15] conducted a comprehensive EMHD analysis of radiative second-grade nanofluids over a Riga plate, incorporating Lorentz force, thermal radiation, and thermophoresis using a revised Buongiorno model. Chamkha and Pop[11] studied thermophoretic particle deposition in natural convection along a porous vertical plate, highlighting its influence on concentration profiles. Gorla *et al.*[17] explored mixed convection of nanofluids over a wedge, accounting for Brownian motion, thermophoresis, and buoyancy effects to assess variations in Nusselt and Sherwood numbers. Krishna *et al.*[29] analyzed heat and mass transfer in micropolar fluid flow past a vertical porous plate under an inclined magnetic field with Hall effects, reporting that heat and mass transfer rates increased with Prandtl number and chemical reaction parameter, respectively. In a related study, Krishna *et al.*[28] examined unsteady MHD convective rotating flow of a second-grade fluid, concluding that velocity rose with Hall and ion slip parameters, while mass transfer was enhanced by the chemical reaction parameter. Recent advances in hybrid nanofluids have shown significant improvements in heat and mass transfer, especially under the influence of MHD and nonlinear radiation effects.[52] Such studies provide useful insights for industrial thermal management applications. Mohanty *et al.*[37] investigated 3D tri-hybrid nanofluid flow over a rotating disk with shape-based nanoparticles and nonlinear thermal effects, reporting enhanced entropy generation and heat transfer, particularly with platelet-shaped nanoparticles. Mohanty *et al.*[36] further analyzed cross-ternary hybrid nanofluid flow over a stretching cylinder under nonlinear radiation, highlighting entropy optimization and improved thermal behavior for various industrial applications.

Stratification plays a vital role in determining the distribution of mass and thermal energy. Stratification is the process by which a fluid separates into distinct layers with different densities caused by temperature, solute concentration, or microbiological content differences. This theory has been extensively applied in diverse sectors, such as environmental, agricultural, medicinal, and industrial research. Stratification is evident in several environments, ranging from water bodies such as lakes and oceans to air conditions, and it has a significant impact on critical environmental processes. It has a substantial effect on the quantities of oxygen and hydrogen in the atmosphere and water. It plays a crucial role in controlling phenomena, including hypoxia, algal blooms, and the preservation of water quality in aquatic ecosystems. Kumar *et al.*[31] investigated stratified Carreau and Casson nanofluid flows in a Darcy–Forchheimer permeable medium. The solution was obtained using the optimal homotopy analysis method (OHAM). Naz *et al.*[39] considered the stratified MHD Carreau nanofluid with gyrotactic microorganisms via a flat cylinder. Gopal *et al.*[16] discussed the thermally stratified Carreau nanofluid MHD flow with heat source/sink over a porous cylinder. Irfan *et al.*[22] scrutinized the stratification phenomenon in the mixed convected flow of 3D Carreau nanofluid with Brownian and thermophoresis properties. Khashi'ie *et al.*[26] looked at the effect of dual stratification on MHD stagnation point flow across a shrinking/stretching surface. Bilal and Ashbar[7] analyzed the mixed convection flow of a linearly stratified sheet of Eyring–Powell fluid. Khan *et al.*[25] examined the fluctuations in the thickness of the Carreau nanofluid due to a dual stratified medium. The shooting method was utilized to simulate the respective profiles. Zari *et al.*[59] studied a stratified Casson nano-liquid with a Marangoni boundary layer. Enhancement of the Marangoni parameter alters the velocity

of the nano-liquid. Sadique *et al.*[45] deliberated the melting phenomenon of thermally stratified Eyring–Powell fluid with Joule heating. The temperature is a decelerating function that accelerates the melting parameter, while the velocity shows inverse behavior against the melting parameter.

Bayesian regularized artificial neural networks (BR-BPNN) offer greater resilience than traditional backpropagation networks and can minimize or eliminate the need for extensive cross-validation processes. Applying Bayesian regularization transforms nonlinear regression into a well-posed statistical problem akin to ridge regression. BRA-NNs are sturdy and remove the requirement for validation procedures that typically scale as $O(N^2)$ in conventional regression techniques. These networks tackle challenges in QSAR modeling, including model selection, robustness, validation set determination, and network architecture optimization. They resist overtraining, as evidence procedures provide an objective Bayesian standard for halting training. BR-BPNNs resist overfitting because they compute and train on a set of effective network parameters, deactivating irrelevant ones. This effective parameter count is generally less than the weights in a standard fully connected backpropagation neural network. Automatic relevance determination of input variables can be employed with BR-BPNN, enabling the network to assess the significance of each input. Sayed *et al.*[5] conducted a study on the BR-BPNN model to predict how $Al_2O_3-Fe_2O_3$ hybrid nanofuels impact the performance and emissions of diesel engines. Sabir *et al.*[46] studied the language learning system by BR-BPNN. Hasaan *et al.*[20] conducted a performance evaluation of various training functions utilizing BR-BPNN to predict the thermal conductivity of EG/water-based GNP/CNC hybrid nanofluid for applications in heat transfer. Darvesh *et al.*[12] conducted a study on the prediction of thermal transport in polymer-based ternary radiative Carreau nanofluids subjected to extreme shear rates over a bullet surface, utilizing an advanced artificial neural network computational approach. Parida *et al.*[41] used a multilayer neural network to model 3D ternary nanofluid flow with entropy analysis in a spinning disk reactor. Their artificial neural network approach accurately captured nonlinear effects and validated thermal predictions. For more applications of BR-BPNN, see, for instance, the Refs. 5, 12, 20, 21, 44, and 46.

Regression analysis is the preferred technique to forecast continuous variables when dealing with multiple input variables. It frequently offers precise estimates of the causal relationship between each input and result, and an error estimate provided by an optimization algorithm.[55] In 1894, Sir Francis Galton introduced the idea of linear regression. Duan *et al.*[13] employed a method inspired by Gaussian process regression (GPR) to assess the consistency between experimental results and CFD simulations. Benemeri *et al.*[6] conducted a study that applied computational fluid dynamics and shape analysis to patient images. This was done to extract additional features using five ridge-constrained logistic regression models, which were then used to classify the rupture status of aneurysms. Carlucci *et al.*[10] investigated the adjustment of an algebraic model for separated flows using Bayesian lasso regression. Sorgan *et al.*[54] conducted a study on support vector regression (SVR) and computational fluid dynamics modeling of Newtonian and non-Newtonian fluids within an annulus, considering the rotation of the pipe. Muhammad *et al.*[2] explored predictive modeling techniques for solar thermal energy systems, focusing on the comparative analysis of SVR, random forests, extra trees, and regression trees. Gupta *et al.*[18] concentrated on developing a machine-learning model utilizing the extra tree regressor and tree-structured Parzen estimator to predict the Nusselt number in nanofluids. Sanhueza *et al.*[50] concentrated on employing machine learning techniques to predict local skin friction factors and Nusselt numbers in turbulent flows over rough surfaces. For further applications of regression analysis in the evaluation of the skin friction, the Nusselt number, and the Sherwood number, refer to Refs. 30, 32, 33, 42, and 47. The literature survey indicates that no prior study has explored the magnetized Carreau nanofluid flow incorporating multiple velocity slip conditions and MgO nanoparticles dispersed in milk over a stretching surface using a regression-based, data-driven framework. In particular, this work presents a novel combination of advanced physics modeling and machine learning regression analysis, which, to the best of our knowledge, has not been reported in existing studies. The following points summarize the key novelty and contributions of this research:

- A new physical configuration is considered involving multiple slip flow effects, magnetic field influence, and MgO nanoparticles suspended in milk, a biologically relevant and thermally enhanced base fluid, within a Carreau non-Newtonian nanofluid framework.
- A data-driven approach is introduced by developing a Bayesian-regularized backpropagation neural network (BR-BPNN) to approximate the numerical solution of the highly nonlinear boundary value problem, with reference data generated using the three-stage Lobatto IIIa implicit Runge–Kutta method (MATLAB `bvp4c`).
- The study uniquely investigates the generalization capability and robustness of the BR-BPNN model by introducing controlled Gaussian noise (0% to 5%) to the test data only, and evaluating predictive accuracy through relative Euclidean norm errors.
- For the first time, the behavior of key engineering quantities (skin friction, Nusselt number, Sherwood number) is predicted and analyzed using six different supervised regression models, three linear (linear, ridge, and lasso) and three nonlinear (support vector regression, Gaussian process regression, decision tree), offering comparative insights into the performance of statistical learning techniques on physically derived datasets.
- The integration of multiple regression models with physics-based flow modeling establishes a hybrid computational framework, offering not only high-fidelity prediction but also interpretable and fast surrogates for engineering design and control under uncertainty.

The proposed problem has significant applications in biothermal and industrial processes where non-Newtonian base fluids like milk are used as transport mediums with suspended nanoparticles to enhance heat and mass transfer. Specifically, the use of MgO nanoparticles in milk models the development of biocompatible cooling fluids for food processing equipment, pharmaceutical mixing units, and magnetically controlled drug delivery systems. The presence of multiple velocity slip effects over a stretching

surface simulates high-speed extrusion, spin coating, and stretching of bio-polymer films. Additionally, the incorporation of magnetic field effects enables direct relevance to magnetohydrodynamic (MHD) flow control in microfluidic devices and lab-on-chip systems. This study thus provides a predictive framework for optimizing flow behavior, entropy generation, and surface transport characteristics in advanced thermal management and biomedical technologies.

The structure of this paper is as follows: Sec. II presents the mathematical modeling and problem statements. Section III comprises two subsections that detail the numerical procedure for addressing the flow problem and provide a concise overview of BR-BPNN. Section IV examines the impact of key parameters on the flow problem, employing the bvp4c, BR-BPNN, and both linear and nonlinear regression analyses. Section V concludes the study and suggests directions for future research.

II. MATHEMATICAL MODELING AND STATEMENT OF THE PROBLEM

We continue from the law of conservation of mass, momentum, energy, and concentration in steady and incompressible form[49]

$$\nabla \cdot \mathbf{u} = 0, \tag{1}$$

$$\rho(\mathbf{u} \cdot \nabla \mathbf{u}) = \nabla \cdot \tau + \rho b, \tag{2}$$

$$\rho c_p(\mathbf{u} \cdot \nabla T) = k\nabla^2 T + \Theta, \tag{3}$$

$$\mathbf{u} \cdot \nabla C = D\nabla^2 C + \Phi, \tag{4}$$

where ρ signifies the density; c_p denotes specific heat; b and k represent applied body forces and thermal conductivity, respectively; Θ is viscous dissipation term; and Φ portrays the chemical reaction inside the medium; τ is the Cauchy stress tensor; and $\mathbf{u}, T$, and C refer for velocity vector field, temperature, and concentration, individually. The Cauchy stress tensor for the Carreau fluid model is as follows[48]

$$\tau = -p\mathbf{I} + \mu A_1, \tag{5}$$

where

$$\mu = \mu_\infty + (\mu_0 - \mu_\infty)(1 + (\lambda\dot{\gamma})^2)^{\frac{n-1}{2}}.$$

Here, p is used for pressure; $\mathbf{I}$ represents identity tensor; μ_∞ and μ_0 signify the viscosity at infinite and zero shear rate, respectively; n stands for the power law index; and shear rate is presented as

$$\dot{\gamma} = \sqrt{\frac{1}{2}\sum_j \sum_j \dot{\gamma}_{ij}\dot{\gamma}_{ji}} = \sqrt{\frac{1}{2}\mathbf{M}} = \sqrt{\frac{1}{2}\mathrm{tr}(A_1^2)}, \tag{6}$$

where $\mathbf{M}$ represents the second invariant strain rate tensor and the deformation tensor

$$A_1 = \nabla \mathbf{u} + (\nabla \mathbf{u})^\top,$$

plugging (6) into (5), we obtain

$$\tau = -p\mathbf{I} + \mu_0(\beta + (1-\beta)\left[1 + (\lambda\dot{\gamma})^2\right]^{\frac{n-1}{2}})A_1, \tag{7}$$

where β denotes the ratio of infinite to zero shear rate viscosity ratio.

We examine the flow of an incompressible, steady, and MHD Carreau nanofluid over a stretching sheet near the stagnation point. The magnetic field B_0 is angled at α. The sheet is stretched at a velocity $u = u_w$, inducing fluid flow. We consider Joule heating, solutal, and thermal stratification to analyze heat and mass transport behavior with melting. In the melting process, the melting temperature is higher than the surrounding temperature ($T_m > T_\infty$), and the melting concentration surpasses the ambient concentration ($C_m > C_\infty$). Various slip conditions for temperature and concentration are taken into account. MgO nanoparticles are dispersed in a milk base fluid. The list of assumptions that are considered in this model are as follows:

- Slip (Robin-type) boundary conditions for both temperature and concentration.
- Pressure gradients are balanced by external flow $u_\infty(x)$.
- External flow is linearly stagnation-type.
- Magnetic Reynolds number is small; no induced magnetic field is considered.
- Radiative heat transfer is neglected.
- Boundary layer approximation is applied.

The primary equations for this model, using (1)–(7) and the boundary layer approximation, can be expressed in component form as

$$\frac{\partial u}{\partial x} + \frac{\partial v}{\partial y} = 0, \tag{8}$$

$$\rho_{nf}\left(u\frac{\partial u}{\partial x} + v\frac{\partial u}{\partial y}\right) = u_\infty \frac{du_\infty}{dx} + \mu_{0nf}\frac{\partial^2 u}{\partial y^2}\left(\beta + (1-\beta)\right.$$
$$\left.\times\left[1 + \lambda^2\left(\frac{\partial u}{\partial y}\right)^2\right]^{\frac{n-1}{2}}\right) + \mu_{0nf}(1-\beta)$$
$$\times (n-1)\lambda^2\frac{\partial^2 u}{\partial y^2}\left(\frac{\partial u}{\partial y}\right)^2\left[1 + \lambda^2\left(\frac{\partial u}{\partial y}\right)^2\right]^{\frac{n-3}{2}}$$
$$- \sigma_{nf}B_o^2 \sin^2\alpha(u - u_\infty), \tag{9}$$

$$(\rho c_p)_{nf}\left(u\frac{\partial T}{\partial x} + v\frac{\partial T}{\partial y}\right) = k_{nf}\frac{\partial^2 T}{\partial y^2} + \mu_{0nf}\left(\frac{\partial u}{\partial y}\right)^2$$
$$\times\left(\beta + (1-\beta)\left[1 + \lambda^2\left(\frac{\partial u}{\partial y}\right)^2\right]^{\frac{n-1}{2}}\right)$$
$$+ \sigma_{nf}B_o^2(u - u_\infty)^2 + Q(T - T_\infty), \tag{10}$$

$$u\frac{\partial C}{\partial x} + v\frac{\partial C}{\partial y} = D_{nf}\frac{\partial^2 C}{\partial y^2} - K_1(C - C_\infty). \tag{11}$$

Boundary conditions,

$$u = u_w(x) = ax, \quad T = T_m + k_1\frac{\partial T}{\partial y}, \quad C = C_m + k_2\frac{\partial C}{\partial y}\, y \to 0$$
$$k_{nf}\left(\frac{\partial T}{\partial y}\right)_{y=0} = \rho_{nf}(\epsilon + c_s(T_m - T_0))v(x,0),$$
$$u = u_\infty(x) = bx, \quad T = T_\infty, \quad C = C_\infty, \quad y \to \infty$$
$$T_m(x) = T_0 + d_1 x, \quad T_\infty(x) = T_0 + d_2 x,$$
$$C_m(x) = C_0 + e_1 x, \quad C_\infty(x) = C_0 + e_2 x. \tag{12}$$

The thermo-physical characteristics of nanoparticles and base fluid (see Table I) are given by[14]

$$\rho_{nf} = (1-\rho)\rho_f + \rho\rho_s, \quad \mu_{0nf} = \frac{\mu_{0f}}{(1-\rho)^{2.5}},$$
$$(\rho c_p)_{nf} = (1-\rho)(\rho c_p)_f + \rho(\rho c_p)_s,$$
$$\frac{k_{nf}}{k_f} = \frac{(k_s+2k_f) - 2\rho(k_f - k_s)}{(k_s+2k_f) + \rho(k_f - k_s)}, \quad \frac{\sigma_{nf}}{\sigma_f} = \frac{(\sigma_s+2\sigma_f) - 2\rho(\sigma_f - \sigma_s)}{(\sigma_s+2\sigma_f) + \rho(\sigma_f - \sigma_s)}.$$

Here, u and v are the velocity components along x axis and y axis, the Carreau fluid relaxation time is λ, the dynamic viscosity μ, the kinematic viscosity is ν, fluid's density ρ, B_0 is the magnetic field, the electrical conductivity is σ, the angle inclination is α, the melting's surface temperature is T_m, the surrounding temperature is T_∞, the melting's surface concentration is C_m, the surrounding concentration is C_∞, the chemical reaction is k_1, the latent heat of the fluid is ϵ, the solid surface heat capacity is c_s, the reference temperature is T_0, the reference concentration is C_0, the volume fraction parameter is ϱ, and d_1, d_2, e_1, and e_2 are dimensional constants.

Introducing the following transformation to transform the above PDE's to ODE's:

$$\zeta = y\sqrt{\frac{a}{\nu_f}}, \quad u = axf'(\zeta), \quad v = -\sqrt{a\nu_f}f(\zeta),$$
$$\theta(\zeta) = \frac{T - T_\infty}{T_m - T_0}, \quad \phi(\zeta) = \frac{C - C_\infty}{C_m - C_0}. \tag{13}$$

Equtaion (8) vanishes while (9)–(12) reduce to

$$B_2 f'''(\beta + (1-\beta)\left[1 + We^2 f''^2\right]^{\frac{n-1}{2}}) + B_2 We^2(1-\beta)$$
$$\times (n-1)f''^2 f'''\left[1 + We^2 f''^2\right]^{\frac{n-3}{2}}$$
$$- B_1(f'^2 - ff'') - B_3 \sin^2\alpha Ha(f' - A) + A^2 = 0, \tag{14}$$
$$B_5\theta'' - PrB_4(s_1 f' + f'\theta - f\theta') + B_2 PrEcf''^2$$
$$\times (\beta + (1-\beta)\left[1 + We^2 f''^2\right]^{\frac{n-1}{2}}) + PrQ^*\theta$$
$$+ B_3 HaEcPr\sin^2\alpha(f' - A)^2 = 0, \tag{15}$$
$$\phi'' - Sc(f'\phi + s_2 f' - f\phi') - ScKr\phi = 0, \tag{16}$$

transformed boundary conditions are

$$f'(0) = 1, \quad Prf(0) + \frac{B_5}{B_1}M_0\theta'(0) = 0, \quad \theta(0) = 1 - s_1 + k'\theta'(0),$$
$$\phi(0) = 1 - s_2 + k''\phi'(0), \quad f'(\zeta) = A, \quad \theta(\zeta) = 0,$$
$$\phi(\zeta) = 0 \ \text{ as } \ \zeta \to \infty, \tag{17}$$

where

$$B_1 = (1-\rho) + \rho * \frac{\rho_s}{\rho_f}, \quad B_2 = (1-\rho)^{-}2.5, \quad We = \lambda u_w\sqrt{\frac{a}{\nu_f}},$$
$$B_3 = \frac{\sigma_{nf}}{\sigma_f}, \quad Ha = \frac{\sigma_f B_0^2}{a\rho_f}, \quad A = \frac{b}{a}, \quad B_4 = (1-\rho) + \rho\frac{(\rho c_p)_s}{(\rho c_p)_f},$$
$$B_5 = \frac{k_{nf}}{k_f}, \quad Pr = \frac{\mu_f(c_p)_f}{Kf}, \quad Q^* = \frac{Q}{a(\rho c_p)_f}, \quad Ec = \frac{u_w^2}{(c_p)_f(T_m - T_0)},$$
$$s_1 = \frac{d_2}{d_1}, \quad Sc = \frac{\nu_f}{D}, \quad s_2 = \frac{e_2}{e_1}, \quad Kr = \frac{K_1}{a}, \quad k' = k_1\sqrt{\frac{a}{\nu_f}},$$
$$k'' = k_2\sqrt{\frac{a}{\nu_f}}, \quad M_0 = \frac{(c_p)_f(T_m - T_0)}{\epsilon + c_s(T_m - T_0)}.$$

Here, Ha represents magnetic parameter, We denotes Weissenberg number, A demonstrates ratio parameter, Ec represents Eckert number, Pr is Prandtl number, Q^* denotes heat source/sink, Sc portrays Schmidt number, K_r is chemical reaction parameter, s_1 and s_2 are, respectively, thermal and solutal stratification, M_0 represents melting parameter, and k' and k'' are thermal and solutal slip parameters, individually.

A. Engineering quantities

The engineering quantities of interest in this problem are skin friction (Cf), the Nusselt number (Nu), and the Sherwood number (Sh). The mathematical expressions for these quantities are

$$Cf = \frac{\mu_{0nf}\dfrac{\partial u}{\partial y}\left(\beta + (1-\beta)\left(1 + \lambda^2\left(\dfrac{\partial u}{\partial y}\right)^2\right)^{\frac{n-1}{2}}\right)}{\rho_f U_w^2},$$
$$Nu = -\frac{k_{nf}}{k_f}\frac{x\left(\dfrac{\partial T}{\partial y}\right)\Big|_{y=0}}{(T_m - T_\infty)}, \quad Sh = -\frac{x\left(\dfrac{\partial C}{\partial y}\right)\Big|_{y=0}}{(C_m - C_\infty)}. \tag{18}$$

The dimensionless form of the above expressions is as follows:

$$Cf(Re_x)^{\frac{1}{2}} = B_2 f''(0)(\beta + (1-\beta)(1 + We^2(f''(0))^2)^{\frac{n-1}{2}}),$$
$$Nu(Re_x)^{-\frac{1}{2}} = -B_5\frac{\theta'(0)}{1 - s_1}, \quad Sh(Re_x)^{-\frac{1}{2}} = -\frac{\phi'(0)}{1 - s_2}. \tag{19}$$

III. METHODS

This section presents a comprehensive guide to resolving (14), (15), and (16), along with the adjusted boundary conditions (17), by employing the bvp4c. Furthermore, it succinctly explains the BR-BPNN algorithm utilized in this study.

A. Numerical scheme

To address the system of nonlinear coupled differential equations (14)–(16), along with the corresponding boundary conditions (17), a numerical approach was developed and executed in MATLAB utilizing the finite-difference collocation method in conjunction with the implicit Runge–Kutta-based solver bvp4c.[27,53] Initially, the original system, which involved higher-order derivatives, was transformed into a system of seven first-order ordinary differential equations

$$
\begin{gathered}
f = y_1, \quad f' = y_2, \quad f'' = y_3, \quad \theta = y_4, \quad \theta' = y_5, \quad \phi = y_6, \quad \phi' = y_7, \\
f''' = \frac{B_1\left(f'^2 - ff''\right) + B_3 \sin^2\alpha\, Ha\,(f' - A) - A^2}{B_2[\beta + (1-\beta)We^2(f'')^2]^{\frac{n-1}{2}} + B_2 We^2(1-\beta)(n-1)(f'')^2[1 + We^2(f'')^2]^{\frac{n-3}{2}}}, \\
\theta'' = \frac{PrB_4\left(s_1 f' + f'\theta - f\theta'\right) - B_2 PrEc(f'')^2(\beta + (1-\beta)[(1 + We^2(f'')^2)]^{\frac{n-1}{2}}) - PrQ^*\theta - B_3 HaEcPr \sin^2\alpha(f' - A)^2}{B_5}, \\
\phi'' = Sc(f'\phi + s_2 f' - f\phi') + ScKr\phi,
\end{gathered}
\tag{20}
$$

and the transformed initial and boundary conditions in MATLAB software are

$$
\begin{gathered}
y_2(0) = 1, \quad y_0 = -\frac{B_5}{B_1 Pr} M_0 y_5(0), \quad y_4(0) = 1 - s_1 + k' y_5(0), \\
y_6(0) = 1 - s_2 + k'' y_7(0), \quad y_2(\infty) = A, \quad y_4(\infty) = 0, \quad y_\infty = 0.
\end{gathered}
\tag{21}
$$

The bvp4c solver was chosen due to its robustness in managing stiff and nonlinear boundary-value problems. It is based on the three-stage Lobatto IIIa implicit Runge–Kutta method and is noted for its high accuracy and excellent stability properties. The computational domain $[0, 3]$ was discretized into 700 equally spaced nodes, resulting in a mesh size of approximately $\Delta\zeta \approx 0.004\,29$. A constant initial guess was applied across all solution components to initialize the solver. During the computation, the Jacobian matrix was not manually defined; instead, bvp4c internally approximated it through finite-difference schemes. This approach was highly effective in ensuring numerical convergence and maintaining the integrity of the nonlinear boundary-layer profiles under investigation. In conclusion, transforming the governing system into a first-order form and its numerical integration using MATLAB's bvp4c solver provides a reliable framework for obtaining accurate solutions to the modeled physical problem.

B. Bayesian regularization backpropagation neural network (BR-BPNN)

This subsection presents the BR-BPNN framework and the associated learning algorithm based on Bayesian regularization. For comprehensive details, refer to Refs. 9 and 19. The BR-BPNN is employed to improve generalization and mitigate overfitting during network training.[9,34] Consider a dataset T_{training} consisting of u_i input–output vector pairs

$$
T_{\text{training}} = \left\{(\mathbf{a}_1, \mathbf{b}_1), (\mathbf{a}_2, \mathbf{b}_2), \ldots, (\mathbf{a}_{u_i}, \mathbf{b}_{u_i})\right\}. \tag{22}
$$

The prediction error for each input $\mathbf{a}_p$ is defined as $\mathbf{e}_p = \mathbf{b}_p - \hat{\mathbf{b}}_p$, where $\hat{\mathbf{b}}_p$ is the network's output. The performance of the network is evaluated using the total squared error, formulated as the cost function

$$
H(\mathbf{w}) = E_{T_{\text{training}}} = \sum_{p=1}^{u_i} (\mathbf{e}_p)^T (\mathbf{e}_p) = \sum_{p=1}^{u_i} ||\mathbf{b}_p - \hat{\mathbf{b}}_p||^2, \tag{23}
$$

where $\mathbf{w} \in \mathbb{R}^L$ contains all weights and biases in the network. To regularize the training and prevent overfitting, a penalty term on the magnitude of weights is added

$$
H(\mathbf{w}) = \mu E_w + \vartheta E_{T_{\text{training}}}, \quad \text{where} \quad E_w = \mathbf{w}^T\mathbf{w}. \tag{24}
$$

Here, μ and ϑ are regularization parameters. When $\mu \ll \vartheta$, the training error dominates, and when $\mu \gg \vartheta$, weight minimization dominates.[24] Bayesian regularization determines optimal μ and ϑ by maximizing the posterior probability of the weights

$$
P(\mathbf{w}|T_{\text{training}}, \mu, \vartheta, I_J) = \frac{P(T_{\text{training}}|\mathbf{w}, \vartheta, I_J)\, P(\mathbf{w}|\mu, I_J)}{P(T_{\text{training}}|\mu, \vartheta, I_J)}, \tag{25}
$$

where I_J denotes the network model structure. Assuming Gaussian noise in the training data

$$
P(T_{\text{training}}|\mathbf{w}, \vartheta, I_J) = \frac{\exp(-\vartheta E_{T_{\text{training}}})}{(\pi/\vartheta)^{\frac{u_i J_u}{2}}}, \quad P(\mathbf{w}|\mu, I_J) = \frac{\exp(-\mu E_w)}{(\pi/\mu)^{L/2}}. \tag{26}
$$

Combining these gives the posterior

$$
\begin{gathered}
P(\mathbf{w}|T_{\text{training}}, \mu, \vartheta, I_J) = \frac{\exp(-G(\mathbf{w}))}{(\pi/\vartheta)^{\frac{u_i J_u}{2}}(\pi/\mu)^{L/2}}, \\
G(\mathbf{w}) = \mu E_w + \vartheta E_{T_{\text{training}}}.
\end{gathered}
\tag{27}
$$

The regularization parameters μ and ϑ are optimized by maximizing the marginal likelihood

$$
P(\mu, \vartheta|T_{\text{training}}, I_J) = \frac{P(T_{\text{training}}|\mu, \vartheta, I_J)\, P(\mu, \vartheta|I_J)}{P(T_{\text{training}}|I_J)}. \tag{28}
$$

Using a Laplace approximation around the optimal weights $\mathbf{w}^*$, the posterior is approximated as a Gaussian

$$
P(\mathbf{w}|T_{\text{training}}, \mu, \vartheta, I_J) \approx \mathcal{N}(\mathbf{w}^*, (\mathbf{H}^*)^{-1}), \tag{29}
$$

where $\mathbf{H}^* \approx \mathbf{J}^T\mathbf{J}$ is the Gauss–Newton approximation of the Hessian and $\mathcal{N}$ denotes a multivariate normal (Gaussian) distribution. This gives the optimal regularization parameters

$$
\mu^* = \frac{\gamma}{2E_w(\mathbf{w}^*)}, \quad \vartheta^* = \frac{u_i J_u - \gamma}{2E_{T_{\text{training}}}(\mathbf{w}^*)}, \tag{30}
$$

with the effective number of parameters

$$
\gamma = L - \mu^* \text{tr}((\mathbf{H}^*)^{-1}). \tag{31}
$$

TABLE I. Thermophysical properties of MgO nanoparticles and milk as a base fluid. Data compiled from Refs. 8, 40, and 51.

Physical properties	$\rho\left(\frac{\text{kg}}{\text{m}^3}\right)$	$c_p\left(\frac{\text{J}}{\text{kg}\cdot\text{K}}\right)$	$k\left(\frac{\text{W}}{\text{m}\cdot\text{K}}\right)$	$\sigma\left(\frac{\text{S}}{\text{m}}\right)$
MgO (nanoparticles)	3585	903	48.4	1.42×10^{-3}
Milk (base fluid)	1030	3930	0.5369	0.55

The Levenberg–Marquardt (LM) algorithm updates weights as

$$\mathbf{w}^{k+1} = \mathbf{w}^k - \left(\mathbf{J}^T\mathbf{J} + \tau\mathbf{I}\right)^{-1}\mathbf{J}^T\mathbf{e}, \tag{32}$$

where τ is the damping factor. By integrating Bayesian inference with LM optimization, BR-BPNN balances error minimization with model complexity, yielding robust generalization performance while avoiding overfitting.

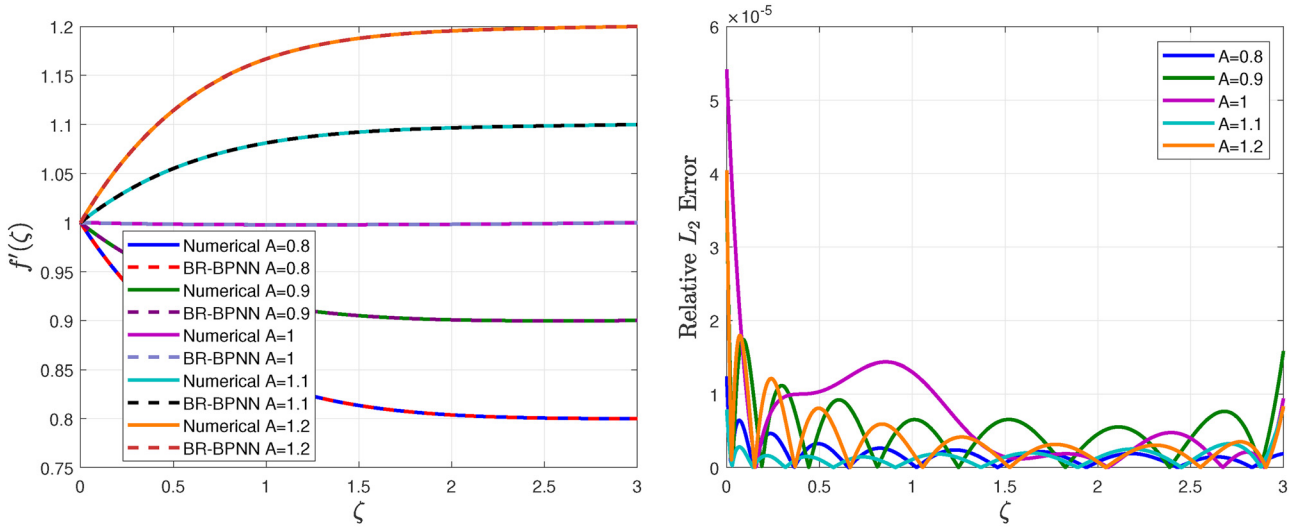

(a) Numerical and BR-BPNN (b) Error

FIG. 1. Velocity for varying A and other parameters are fixed.

TABLE II. Relative $\mathbf{L}_2$ errors for different hidden layers and activation functions for Fig. 1.

Activation	Hidden layers	Train	Test (0%)	Test (1%)	Test (2%)	Test (3%)	Test (4%)	Test (5%)
Tansig	[5,5,5]	2.997×10^{-5}	3.302×10^{-5}	5.866×10^{-3}	1.245×10^{-2}	1.619×10^{-2}	2.156×10^{-2}	2.559×10^{-2}
tansig	[10,10,10]	5.898×10^{-5}	6.972×10^{-5}	5.598×10^{-3}	1.174×10^{-2}	1.548×10^{-2}	2.163×10^{-2}	2.821×10^{-2}
Tansig	[15,15,15]	4.916×10^{-5}	5.988×10^{-5}	5.922×10^{-3}	1.193×10^{-2}	1.687×10^{-2}	2.369×10^{-2}	2.635×10^{-2}
Tansig	[5,5,5,5,5]	2.837×10^{-5}	3.912×10^{-5}	5.765×10^{-3}	1.080×10^{-2}	1.637×10^{-2}	2.239×10^{-2}	2.565×10^{-2}
Tansig	[10,10,10,10,10]	1.687×10^{-5}	2.023×10^{-5}	5.467×10^{-3}	1.319×10^{-2}	1.644×10^{-2}	2.453×10^{-2}	2.851×10^{-2}
Tansig	[15,15,15,15,15]	2.256×10^{-5}	5.558×10^{-5}	5.974×10^{-3}	1.140×10^{-2}	1.663×10^{-2}	2.192×10^{-2}	2.836×10^{-2}
Logsig	[5,5,5]	2.615×10^{-5}	2.714×10^{-5}	5.789×10^{-3}	1.086×10^{-2}	1.701×10^{-2}	2.304×10^{-2}	2.758×10^{-2}
Logsig	[10,10,10]	3.047×10^{-5}	5.515×10^{-5}	5.654×10^{-3}	1.090×10^{-2}	1.850×10^{-2}	2.326×10^{-2}	2.763×10^{-2}
Logsig	[15,15,15]	7.214×10^{-5}	1.102×10^{-4}	6.023×10^{-3}	1.111×10^{-2}	1.793×10^{-2}	2.187×10^{-2}	3.043×10^{-2}
Logsig	[5,5,5,5,5]	3.241×10^{-5}	3.308×10^{-5}	5.525×10^{-3}	1.184×10^{-2}	1.697×10^{-2}	2.181×10^{-2}	2.805×10^{-2}
Logsig	[10,10,10,10,10]	2.859×10^{-5}	3.311×10^{-5}	5.701×10^{-3}	1.016×10^{-2}	1.559×10^{-2}	2.296×10^{-2}	2.614×10^{-2}
Logsig	[15,15,15,15,15]	3.351×10^{-5}	4.239×10^{-5}	6.218×10^{-3}	1.169×10^{-2}	1.739×10^{-2}	2.384×10^{-2}	2.885×10^{-2}
ReLu	[5,5,5]	6.439×10^{-2}	6.502×10^{-2}	6.540×10^{-2}	6.592×10^{-2}	6.806×10^{-2}	6.663×10^{-2}	7.287×10^{-2}
ReLu	[10,10,10]	3.854×10^{-3}	4.788×10^{-3}	7.453×10^{-3}	1.269×10^{-2}	1.838×10^{-2}	2.401×10^{-2}	2.860×10^{-2}
ReLu	[15,15,15]	1.361×10^{-3}	1.680×10^{-3}	5.666×10^{-3}	1.211×10^{-2}	1.609×10^{-2}	2.243×10^{-2}	2.719×10^{-2}
ReLu	[5,5,5,5,5]	1.691×10^{-3}	1.951×10^{-3}	5.555×10^{-3}	1.241×10^{-2}	1.827×10^{-2}	2.346×10^{-2}	2.873×10^{-2}
ReLu	[10,10,10,10,10]	1.983×10^{-3}	2.594×10^{-3}	6.639×10^{-3}	1.164×10^{-2}	1.627×10^{-2}	2.174×10^{-2}	2.986×10^{-2}
ReLu	[15,15,15,15,15]	8.390×10^{-4}	9.730×10^{-4}	5.830×10^{-3}	1.204×10^{-2}	1.690×10^{-2}	2.299×10^{-2}	2.972×10^{-2}

C. Validation using Bayesian regularization-backpropagation neural network

The primary objective of this subsection is to validate the numerical scheme for the nonlinear system (20), along with the initial and boundary conditions (21), by comparing its solutions with those obtained using the BR-BPNN across various parameter settings.

The system was first solved using MATLAB's `bvp4c` solver to generate high-fidelity reference data. Key dimensionless parameters, A, M_0, We, Ec, and Sc, were varied individually, and for each case, the BVP was evaluated over 700 discretized points in the similarity variable ζ. This yielded 700 input–output samples per parameter. A separate BR-BPNN was trained for each parameter using only that parameter and ζ as inputs. The dataset was divided into 70% for training and 30% for testing.

The BR-BPNN architecture comprised three hidden layers with 10 neurons each, using `tansig` activation functions, and consisted of 261 trainable parameters (weights and biases). This structure was found adequate to capture the nonlinear system dynamics with high accuracy. Model performance was assessed by comparing neural network predictions with the numerical reference solutions using the relative $\mathbf{L}_2$ error norm

$$\text{Relative-}\mathbf{L}_2 \text{ error} = \frac{||\hat{\mathbf{h}} - \mathbf{h}||_2}{||\mathbf{h}||_2} = \frac{\sqrt{\sum_i (\hat{h}_i - h_i)^2}}{\sqrt{\sum_i h_i^2}},$$

where $\hat{\mathbf{h}}$ and $\mathbf{h}$ denote the predicted and reference solutions, respectively. This comparison demonstrated the model's robustness and

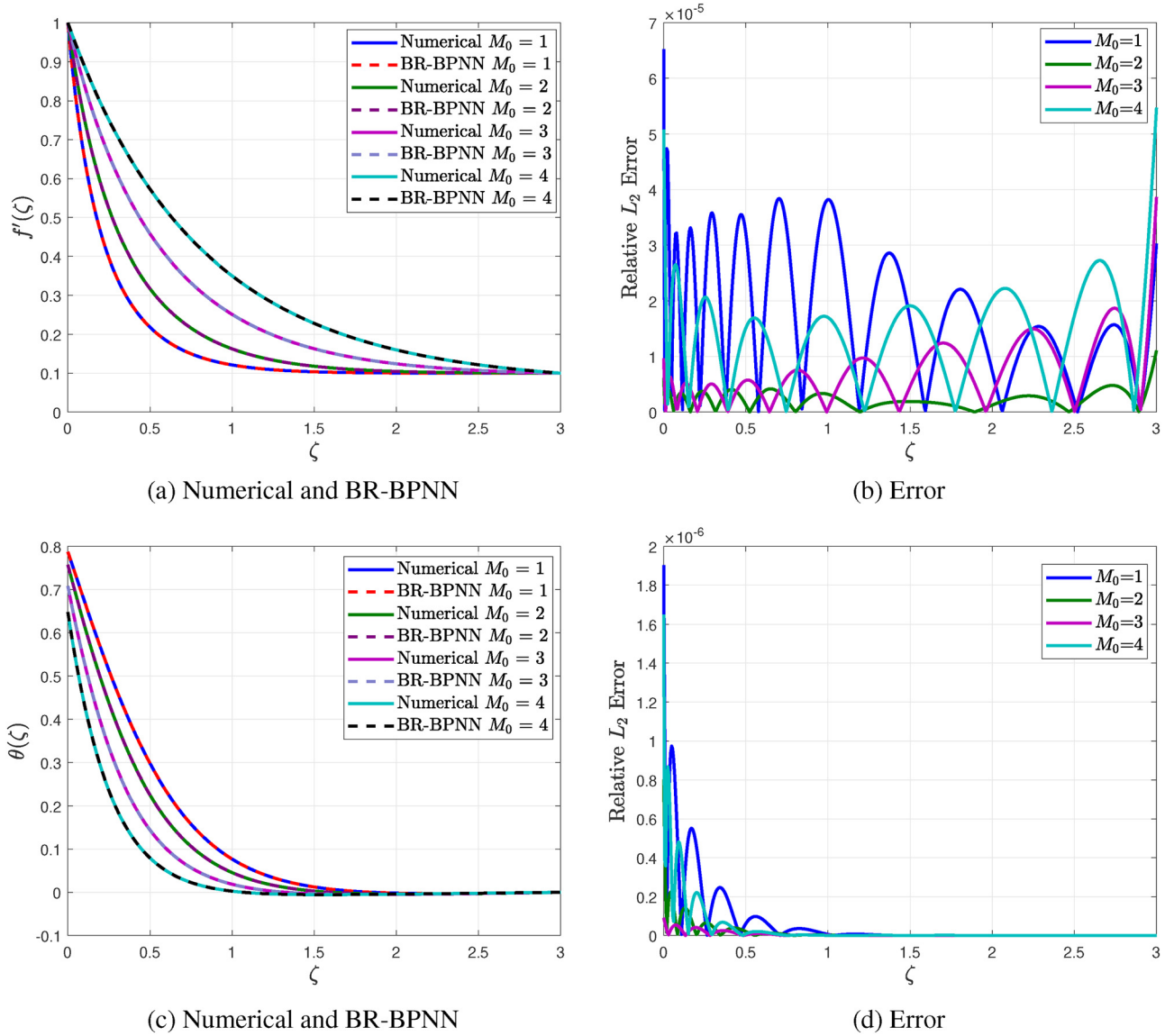

FIG. 2. Velocity and temperature for varying M_0 and other parameters are fixed.

reliability in approximating the velocity, temperature, and concentration profiles (Table I).

IV. GRAPHICAL DISCUSSIONS

This section investigates the influence of various parameters on velocity, temperature, and concentration profiles, utilizing the bvp4c and BR-BPNN methodologies. The impact of these parameters is further analyzed through a range of linear and nonlinear regression models. Milk shows the non-Newtonian shear thinning behavior when $n = -0.803, \lambda = 0.579\,\text{s}, \mu_0 = 79.03\,mPa\,s, \mu_\infty = 1.75\text{mPas}$, and $\beta = 0.022$.[4] The Prandtl number (Pr) of milk is ≈ 21.96.[8]

A. Discussion for the velocity, temperature, and concentration profiles

The influence of the ratio parameter on velocity is shown in Fig. 1. An analysis of the velocity profile indicated that it is an increasing function concerning A. Furthermore, the behavior of the thickness of the velocity diffusion layer is either dominant or recessive in comparison with stretching, which contrasts with the behavior of the free-stream velocity. A boundary layer is absent when $A = 0$ as the fluid and wall move at identical speeds. For $A < 1$, the velocity is more incredible away from the wall, whereas for $A > 1$, the velocity is more incredible at the wall surface. Figure 1(a) compares the BR-BPNN predictions and reference numerical solutions for various values of A, demonstrating excellent concordance. The corresponding relative $\mathbf{L}_2$ error plot in Fig. 1(b) corroborates the high accuracy of the BR-BPNN model, with the errors consistently remaining below 6×10^{-5} across the domain. Table II summarizes the BR-BPNN performance for Fig. 1 across different activation functions and hidden layer settings under Gaussian noise levels from 0% to 5%. While all models maintain low relative $\mathbf{L}_2$ errors on clean data, networks using `logsig` and `tansig` activations show better robustness under noise. In contrast, `ReLU`-based models exhibit higher test errors, indicating less stable generalization in noisy environments. Figure 2(a) illustrates the effect of the melting parameter M_0 on the velocity profile for the milk–magnesium oxide nanofluid. As M_0 increases, the fluid velocity rises, and the boundary layer thickness becomes larger. Physically, this behavior is attributed to enhanced melting effects that intensify the convective transport toward the cooling surface, accelerating the flow field. The corresponding relative $\mathbf{L}_2$ error plot in Fig. 2(b) confirms the accuracy of the BR-BPNN predictions across different values of M_0, with errors remaining below 7×10^{-5}. Table III reports the relative $\mathbf{L}_2$ errors of the BR-BPNN across multiple activation functions and hidden layer depths for the velocity and magnetic field solutions shown in Fig. 2. Although the network performs well on noise-free data, the `logsig` and `tansig` activations consistently demonstrate greater resilience to increasing noise levels compared to `ReLU`. These findings confirm the importance of activation function choice in ensuring stable generalization under uncertainty. Figure 3(a) presents the effect of the We on the nanofluid velocity profile. An increase in We results in a noticeable decrease in velocity, which is physically due to the dominance of elastic behavior and enhanced relaxation time, leading to higher viscosity and stronger resistance to flow. The BR-BPNN model accurately captures this behavior across all We values, as shown by the excellent agreement with numerical results. The relative $\mathbf{L}_2$ error in the Fig. 3(b) remains below 1.2×10^{-5} throughout the domain, confirming the model's precision. Table IV illustrates the relative $\mathbf{L}_2$ errors of the BR-BPNN model for various network architectures and activation functions in predicting the velocity and temperature fields in Fig. 3. While performance on clean data remains excellent, the results show that `tansig` and `logsig` activations retain lower error trends even as noise levels increase. This confirms the model's adaptability in capturing complex nonlinear behaviors with stable accuracy across noisy conditions.

Figure 2(c) illustrates the impact of the melting parameter M_0 on the temperature distribution for a milk–magnesium oxide-based

TABLE III. Relative $\mathbf{L}_2$ errors for different hidden layers and activation functions for Fig. 2.

Activation	Hidden layers	Train	Test (0%)	Test (1%)	Test (2%)	Test (3%)	Test (4%)	Test (5%)
tansig	[5,5,5]	2.869×10^{-5}	3.040×10^{-5}	5.794×10^{-3}	1.111×10^{-2}	1.747×10^{-2}	2.432×10^{-2}	2.791×10^{-2}
tansig	[10,10,10]	3.023×10^{-5}	6.176×10^{-5}	5.297×10^{-3}	1.294×10^{-2}	1.639×10^{-2}	2.336×10^{-2}	2.740×10^{-2}
tansig	[15,15,15]	4.115×10^{-5}	6.475×10^{-5}	5.876×10^{-3}	9.861×10^{-3}	1.881×10^{-2}	2.323×10^{-2}	2.939×10^{-2}
tansig	[5,5,5,5,5]	2.130×10^{-5}	2.526×10^{-5}	5.902×10^{-3}	1.140×10^{-2}	1.775×10^{-2}	2.339×10^{-2}	2.744×10^{-2}
tansig	[10,10,10,10,10]	2.458×10^{-5}	4.038×10^{-5}	5.847×10^{-3}	1.049×10^{-2}	1.706×10^{-2}	2.443×10^{-2}	3.426×10^{-2}
tansig	[15,15,15,15,15]	2.455×10^{-5}	6.041×10^{-5}	5.390×10^{-3}	1.186×10^{-2}	1.743×10^{-2}	2.237×10^{-2}	3.112×10^{-2}
logsig	[5,5,5]	3.624×10^{-5}	3.599×10^{-5}	5.637×10^{-3}	1.090×10^{-2}	1.559×10^{-2}	2.296×10^{-2}	2.784×10^{-2}
logsig	[10,10,10]	5.275×10^{-5}	6.608×10^{-5}	5.212×10^{-3}	1.102×10^{-2}	1.674×10^{-2}	2.065×10^{-2}	2.456×10^{-2}
logsig	[15,15,15]	4.478×10^{-5}	5.972×10^{-5}	5.529×10^{-3}	1.157×10^{-2}	1.779×10^{-2}	2.060×10^{-2}	2.957×10^{-2}
logsig	[5,5,5,5,5]	2.058×10^{-5}	2.466×10^{-5}	6.638×10^{-3}	1.173×10^{-2}	1.794×10^{-2}	2.185×10^{-2}	3.140×10^{-2}
logsig	[10,10,10,10,10]	3.220×10^{-5}	3.673×10^{-5}	5.985×10^{-3}	1.148×10^{-2}	1.758×10^{-2}	2.007×10^{-2}	2.870×10^{-2}
logsig	[15,15,15,15,15]	3.024×10^{-5}	2.523×10^{-4}	6.626×10^{-3}	1.134×10^{-2}	1.794×10^{-2}	2.288×10^{-2}	2.951×10^{-2}
ReLu	[5,5,5]	6.960×10^{-3}	7.651×10^{-3}	9.215×10^{-3}	1.352×10^{-2}	1.803×10^{-2}	2.361×10^{-2}	2.770×10^{-2}
ReLu	[10,10,10]	1.491×10^{-3}	4.433×10^{-3}	7.885×10^{-3}	1.267×10^{-2}	1.720×10^{-2}	2.251×10^{-2}	3.078×10^{-2}
ReLu	[15,15,15]	1.684×10^{-3}	3.036×10^{-3}	6.708×10^{-3}	1.162×10^{-2}	1.818×10^{-2}	2.254×10^{-2}	2.897×10^{-2}
ReLu	[5,5,5,5,5]	5.636×10^{-3}	6.576×10^{-3}	8.801×10^{-3}	1.308×10^{-2}	2.005×10^{-2}	2.383×10^{-2}	2.673×10^{-2}
ReLu	[10,10,10,10,10]	1.424×10^{-3}	1.600×10^{-3}	6.398×10^{-3}	1.137×10^{-2}	1.796×10^{-2}	2.317×10^{-2}	2.883×10^{-2}
ReLu	[15,15,15,15,15]	1.020×10^{-3}	2.055×10^{-3}	6.057×10^{-3}	1.161×10^{-2}	1.654×10^{-2}	2.569×10^{-2}	2.794×10^{-2}

nanofluid. As M_0 increases, the temperature profile decreases, and the thermal boundary layer becomes thicker. Physically, a higher melting parameter enhances the heat transfer rate from the hot fluid to the cold wall, accelerating thermal diffusion and resulting in lower fluid temperatures near the surface. The BR-BPNN model in Fig. 2(c) effectively captures this thermal behavior, demonstrating excellent agreement with the reference numerical solutions for all values of M_0. The corresponding relative $\mathbf{L}_2$ error plot in Fig. 2(d) confirms the high accuracy of the neural network, with error magnitudes consistently below 2×10^{-6} throughout the domain. Figure 3(c) demonstrates the influence of the *We* on the temperature profile of the milk–magnesium oxide nanofluid. As the value of *We* increases, the temperature distribution decreases more rapidly, indicating a reduction in fluid temperature. Physically, a higher Weissenberg number reflects a dominance of elastic effects over viscous effects, leading to the enhanced relaxation time of liquid particles. This increase in relaxation time reduces the fluid's ability to retain heat, decreasing the thermal energy retained within the boundary layer, resulting in a thinner thermal profile and lower overall temperature. Figure 3(c) confirms this trend, showing a decline in temperature with increasing *We*. The BR-BPNN model successfully captures this behavior, aligning closely with the numerical solutions across all *We* values. Figure 3(d) shows the relative $\mathbf{L}_2$ error, which remains consistently below 2×10^{-6} throughout the domain. Figure 4 shows that increasing the *Ec* increases the nanofluid temperature due to enhanced viscous dissipation and heat generation within the fluid. The BR-BPNN predictions closely match the

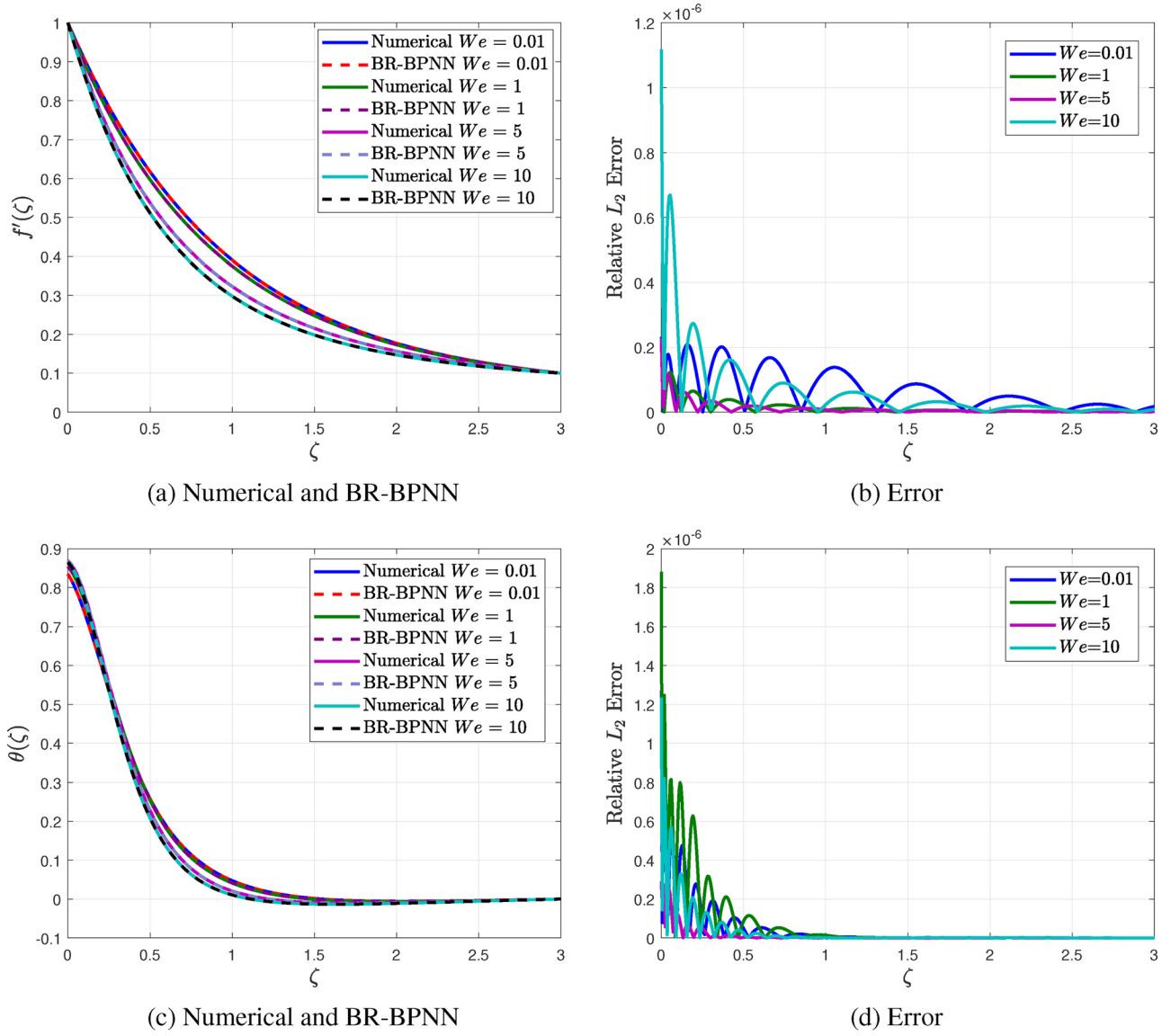

FIG. 3. Velocity and temperature for varying *We* and other parameters are fixed.

TABLE IV. Relative $\mathbf{L}_2$ errors for different hidden layers and activation functions for Fig. 3.

Activation	Hidden layers	Train	Test (0%)	Test (1%)	Test (2%)	Test (3%)	Test (4%)	Test (5%)
tansig	[5, 5, 5]	1.520×10^{-5}	1.858×10^{-5}	5.813×10^{-3}	1.115×10^{-2}	1.753×10^{-2}	2.441×10^{-2}	2.801×10^{-2}
tansig	[10, 10, 10]	4.044×10^{-5}	5.909×10^{-5}	5.313×10^{-3}	1.298×10^{-2}	1.644×10^{-2}	2.343×10^{-2}	2.749×10^{-2}
tansig	[15, 15, 15]	5.929×10^{-5}	9.498×10^{-5}	5.895×10^{-3}	9.900×10^{-3}	1.888×10^{-2}	2.332×10^{-2}	2.950×10^{-2}
tansig	[5, 5, 5, 5, 5]	2.040×10^{-5}	2.441×10^{-5}	5.925×10^{-3}	1.144×10^{-2}	1.782×10^{-2}	2.348×10^{-2}	2.754×10^{-2}
tansig	[10, 10, 10, 10, 10]	2.086×10^{-5}	3.922×10^{-5}	5.864×10^{-3}	1.052×10^{-2}	1.711×10^{-2}	2.450×10^{-2}	3.437×10^{-2}
tansig	[15, 15, 15, 15, 15]	2.460×10^{-5}	6.142×10^{-5}	5.412×10^{-3}	1.190×10^{-2}	1.750×10^{-2}	2.246×10^{-2}	3.124×10^{-2}
logsig	[5, 5, 5]	3.028×10^{-5}	2.992×10^{-5}	5.659×10^{-3}	1.094×10^{-2}	1.566×10^{-2}	2.305×10^{-2}	2.795×10^{-2}
logsig	[10, 10, 10]	6.837×10^{-5}	7.666×10^{-5}	5.232×10^{-3}	1.106×10^{-2}	1.680×10^{-2}	2.072×10^{-2}	2.466×10^{-2}
logsig	[15, 15, 15]	4.250×10^{-5}	5.676×10^{-5}	5.546×10^{-3}	1.160×10^{-2}	1.785×10^{-2}	2.066×10^{-2}	2.966×10^{-2}
logsig	[5, 5, 5, 5, 5]	2.106×10^{-5}	2.520×10^{-5}	6.661×10^{-3}	1.177×10^{-2}	1.800×10^{-2}	2.193×10^{-2}	3.151×10^{-2}
logsig	[10, 10, 10, 10, 10]	1.206×10^{-4}	1.343×10^{-4}	5.988×10^{-3}	1.154×10^{-2}	1.767×10^{-2}	2.016×10^{-2}	2.881×10^{-2}
logsig	[15, 15, 15, 15, 15]	1.408×10^{-4}	1.320×10^{-3}	6.749×10^{-3}	1.134×10^{-2}	1.804×10^{-2}	2.306×10^{-2}	2.956×10^{-2}
ReLu	[5, 5, 5]	5.066×10^{-3}	5.573×10^{-3}	7.636×10^{-3}	1.185×10^{-2}	1.732×10^{-2}	2.320×10^{-2}	2.731×10^{-2}
ReLu	[10, 10, 10]	1.163×10^{-3}	2.187×10^{-3}	6.805×10^{-3}	1.178×10^{-2}	1.684×10^{-2}	2.224×10^{-2}	3.047×10^{-2}
ReLu	[15, 15, 15]	1.205×10^{-3}	2.087×10^{-3}	6.372×10^{-3}	1.123×10^{-2}	1.833×10^{-2}	2.258×10^{-2}	2.910×10^{-2}
ReLu	[5, 5, 5, 5, 5]	4.304×10^{-3}	4.855×10^{-3}	7.301×10^{-3}	1.158×10^{-2}	1.919×10^{-2}	2.355×10^{-2}	2.611×10^{-2}
ReLu	[10, 10, 10, 10, 10]	1.962×10^{-3}	2.094×10^{-3}	6.482×10^{-3}	1.121×10^{-2}	1.825×10^{-2}	2.337×10^{-2}	2.930×10^{-2}
ReLu	[15, 15, 15, 15, 15]	9.228×10^{-4}	1.079×10^{-3}	5.729×10^{-3}	1.130×10^{-2}	1.651×10^{-2}	2.573×10^{-2}	2.810×10^{-2}

numerical results across all *Ec* values as shown in Fig. 4(a), with relative $\mathbf{L}_2$ errors remaining below 2×10^{-6} in Fig. 4(b). Table V showcases the relative $\mathbf{L}_2$ errors of the BR-BPNN architecture for various activation functions and hidden layer configurations when modeling the thermal field presented in Fig. 4. The model exhibits reliable predictive capability across all tested conditions, with `tansig` and `logsig` activations outperforming `ReLU` under noisy scenarios. These results reinforce the network's strength in capturing temperature-related dynamics in the presence of parametric uncertainty.

Figure 5 illustrates the importance of the *Sc* concerning nanofluid concentration. The decaying behavior in nanofluid concentration is investigated for the Schmidt number's intensifying value, as shown in Fig. 5(a). The *Sc* is the ratio of the viscous diffusion rate to the molecular diffusion rate. The relationship between the *Sc* and

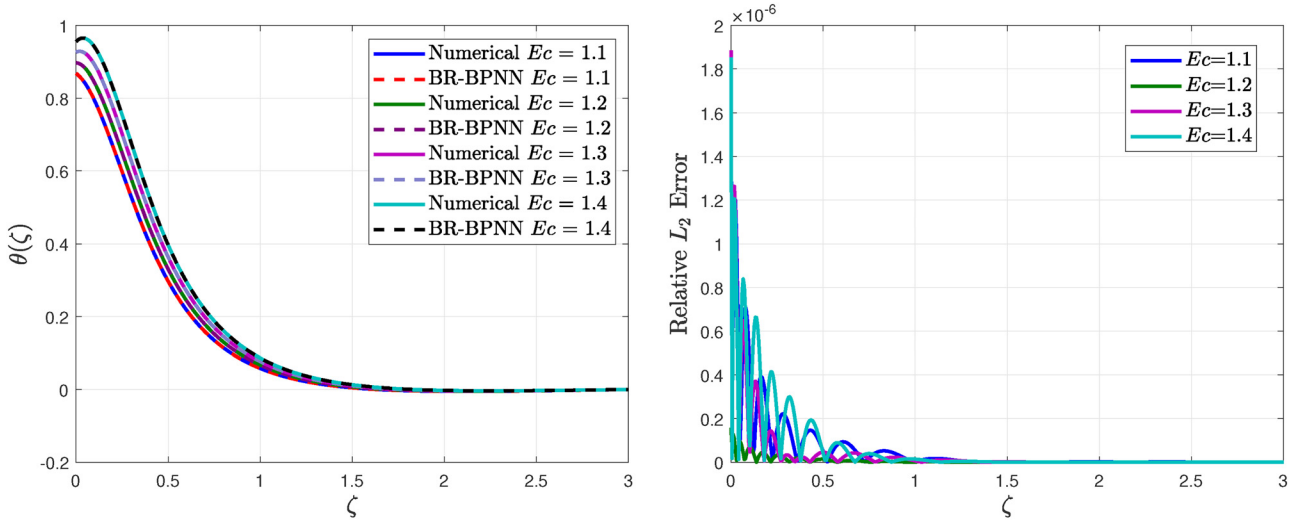

(a) Numerical and BR-BPNN (b) Error

FIG. 4. Temperature for varying *Ec* and other parameters are fixed.

TABLE V. Relative $\mathbf{L}_2$ errors for different hidden layers and activation functions for Fig. 4.

Activation	Hidden layers	Train	Test (0%)	Test (1%)	Test (2%)	Test (3%)	Test (4%)	Test (5%)
tansig	[5, 5, 5]	1.481×10^{-5}	1.797×10^{-5}	5.802×10^{-3}	1.113×10^{-2}	1.750×10^{-2}	2.436×10^{-2}	2.796×10^{-2}
tansig	[10, 10, 10]	4.021×10^{-5}	6.375×10^{-5}	5.305×10^{-3}	1.297×10^{-2}	1.641×10^{-2}	2.340×10^{-2}	2.745×10^{-2}
tansig	[15, 15, 15]	5.927×10^{-5}	9.498×10^{-5}	5.885×10^{-3}	9.884×10^{-3}	1.885×10^{-2}	2.328×10^{-2}	2.945×10^{-2}
tansig	[5, 5, 5, 5, 5]	2.033×10^{-5}	2.443×10^{-5}	5.915×10^{-3}	1.142×10^{-2}	1.779×10^{-2}	2.344×10^{-2}	2.750×10^{-2}
tansig	[10, 10, 10, 10, 10]	2.100×10^{-5}	3.966×10^{-5}	5.855×10^{-3}	1.050×10^{-2}	1.708×10^{-2}	2.446×10^{-2}	3.431×10^{-2}
tansig	[15, 15, 15, 15, 15]	2.459×10^{-5}	6.115×10^{-5}	5.403×10^{-3}	1.188×10^{-2}	1.747×10^{-2}	2.243×10^{-2}	3.119×10^{-2}
logsig	[5, 5, 5]	3.256×10^{-5}	3.234×10^{-5}	5.649×10^{-3}	1.092×10^{-2}	1.563×10^{-2}	2.301×10^{-2}	2.790×10^{-2}
logsig	[10, 10, 10]	6.609×10^{-5}	7.396×10^{-5}	5.223×10^{-3}	1.104×10^{-2}	1.677×10^{-2}	2.069×10^{-2}	2.461×10^{-2}
logsig	[15, 15, 15]	4.356×10^{-5}	5.802×10^{-5}	5.538×10^{-3}	1.159×10^{-2}	1.782×10^{-2}	2.063×10^{-2}	2.962×10^{-2}
logsig	[5, 5, 5, 5, 5]	2.101×10^{-5}	2.508×10^{-5}	6.650×10^{-3}	1.175×10^{-2}	1.797×10^{-2}	2.189×10^{-2}	3.145×10^{-2}
logsig	[10, 10, 10, 10, 10]	1.194×10^{-4}	1.324×10^{-4}	5.978×10^{-3}	1.152×10^{-2}	1.764×10^{-2}	2.012×10^{-2}	2.875×10^{-2}
logsig	[15, 15, 15, 15, 15]	3.895×10^{-5}	3.799×10^{-4}	6.641×10^{-3}	1.136×10^{-2}	1.799×10^{-2}	2.294×10^{-2}	2.956×10^{-2}
ReLu	[5, 5, 5]	5.026×10^{-3}	5.538×10^{-3}	7.601×10^{-3}	1.183×10^{-2}	1.728×10^{-2}	2.318×10^{-2}	2.726×10^{-2}
ReLu	[10, 10, 10]	8.333×10^{-4}	2.611×10^{-3}	7.056×10^{-3}	1.190×10^{-2}	1.689×10^{-2}	2.240×10^{-2}	3.040×10^{-2}
ReLu	[15, 15, 15]	1.826×10^{-3}	2.923×10^{-3}	6.572×10^{-3}	1.156×10^{-2}	1.832×10^{-2}	2.239×10^{-2}	2.893×10^{-2}
ReLu	[5, 5, 5, 5, 5]	4.292×10^{-3}	4.891×10^{-3}	7.351×10^{-3}	1.152×10^{-2}	1.919×10^{-2}	2.349×10^{-2}	2.603×10^{-2}
ReLu	[10, 10, 10, 10, 10]	1.119×10^{-3}	1.522×10^{-3}	6.314×10^{-3}	1.124×10^{-2}	1.790×10^{-2}	2.343×10^{-2}	2.906×10^{-2}
ReLu	[15, 15, 15, 15, 15]	9.150×10^{-4}	3.440×10^{-3}	6.843×10^{-3}	1.208×10^{-2}	1.687×10^{-2}	2.573×10^{-2}	2.862×10^{-2}

the mass diffusivity is inverse. The concentration field degrades as the Schmidt number rises because the nanofluids have less particle diffusion. The BR-BPNN model agrees excellently with the numerical results for all *Sc* values, as shown in Fig. 5(a). The relative $\mathbf{L}_2$ error stays below 2×10^{-6}, indicating high prediction accuracy, as shown in Fig. 5(b). Table VI presents the relative $\mathbf{L}_2$ errors for different activation functions and hidden layer settings in predicting the concentration profile shown in Fig. 5. The BR-BPNN model maintains low error values across both clean and noisy test sets, indicating strong numerical stability. Among the tested configurations, `tansig` and `logsig` activations consistently deliver better generalization, reinforcing the model's suitability for accurate concentration field approximation.

B. Engineering quantities

For each randomly sampled input set, Eq. (19) was solved three times using the parameters specified in Eq. (19). The resulting outputs

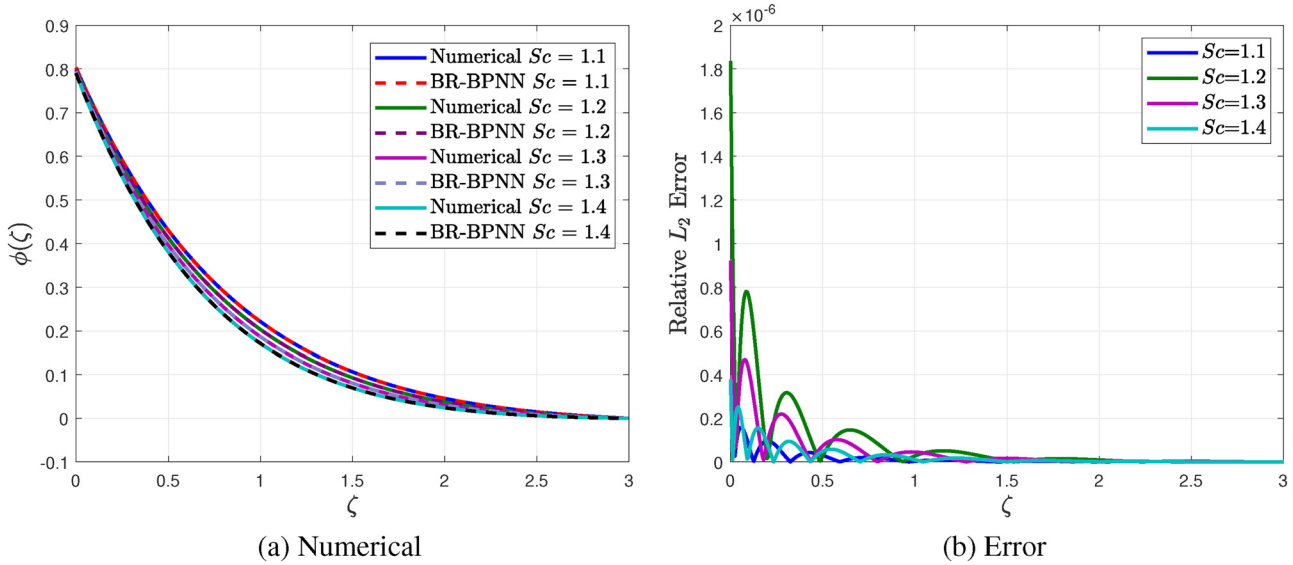

FIG. 5. Concentration for varying *Sc* and other parameters are fixed.

TABLE VI. Relative L_2 errors for different hidden layers and activation functions for Fig. 5.

Activation	Hidden layers	Train	Test (0%)	Test (1%)	Test (2%)	Test (3%)	Test (4%)	Test (5%)
tansig	[5, 5, 5]	1.602×10^{-5}	1.952×10^{-5}	5.820×10^{-3}	1.116×10^{-2}	1.756×10^{-2}	2.445×10^{-2}	2.805×10^{-2}
tansig	[10, 10, 10]	5.795×10^{-5}	8.405×10^{-5}	5.320×10^{-3}	1.302×10^{-2}	1.647×10^{-2}	2.349×10^{-2}	2.755×10^{-2}
tansig	[15, 15, 15]	5.255×10^{-5}	8.503×10^{-5}	5.911×10^{-3}	9.926×10^{-3}	1.894×10^{-2}	2.338×10^{-2}	2.959×10^{-2}
tansig	[5, 5, 5, 5, 5]	1.903×10^{-5}	2.392×10^{-5}	5.949×10^{-3}	1.149×10^{-2}	1.788×10^{-2}	2.357×10^{-2}	2.765×10^{-2}
tansig	[10, 10, 10, 10, 10]	3.206×10^{-5}	4.940×10^{-5}	5.870×10^{-3}	1.055×10^{-2}	1.715×10^{-2}	2.456×10^{-2}	3.444×10^{-2}
tansig	[15, 15, 15, 15, 15]	2.502×10^{-5}	6.403×10^{-5}	5.433×10^{-3}	1.195×10^{-2}	1.757×10^{-2}	2.255×10^{-2}	3.136×10^{-2}
logsig	[5, 5, 5]	4.080×10^{-5}	4.166×10^{-5}	5.673×10^{-3}	1.097×10^{-2}	1.570×10^{-2}	2.311×10^{-2}	2.801×10^{-2}
logsig	[10, 10, 10]	7.302×10^{-5}	8.022×10^{-5}	5.254×10^{-3}	1.109×10^{-2}	1.685×10^{-2}	2.079×10^{-2}	2.474×10^{-2}
logsig	[15, 15, 15]	4.012×10^{-5}	4.993×10^{-5}	5.562×10^{-3}	1.163×10^{-2}	1.789×10^{-2}	2.071×10^{-2}	2.972×10^{-2}
logsig	[5, 5, 5, 5, 5]	2.266×10^{-5}	2.630×10^{-5}	6.679×10^{-3}	1.181×10^{-2}	1.805×10^{-2}	2.199×10^{-2}	3.159×10^{-2}
logsig	[10, 10, 10, 10, 10]	5.469×10^{-5}	6.306×10^{-5}	6.029×10^{-3}	1.156×10^{-2}	1.771×10^{-2}	2.021×10^{-2}	2.890×10^{-2}
logsig	[15, 15, 15, 15, 15]	2.496×10^{-5}	1.373×10^{-4}	6.670×10^{-3}	1.144×10^{-2}	1.807×10^{-2}	2.304×10^{-2}	2.973×10^{-2}
ReLu	[5, 5, 5]	2.047×10^{-2}	2.067×10^{-2}	2.184×10^{-2}	2.431×10^{-2}	2.360×10^{-2}	3.165×10^{-2}	3.556×10^{-2}
ReLu	[10, 10, 10]	2.570×10^{-3}	4.034×10^{-3}	7.688×10^{-3}	1.255×10^{-2}	1.705×10^{-2}	2.248×10^{-2}	3.082×10^{-2}
ReLu	[15, 15, 15]	1.351×10^{-3}	1.779×10^{-3}	6.518×10^{-3}	1.116×10^{-2}	1.835×10^{-2}	2.277×10^{-2}	2.911×10^{-2}
ReLu	[5, 5, 5, 5, 5]	4.726×10^{-3}	5.342×10^{-3}	7.832×10^{-3}	1.200×10^{-2}	1.959×10^{-2}	2.370×10^{-2}	2.604×10^{-2}
ReLu	[10, 10, 10, 10, 10]	3.639×10^{-4}	4.974×10^{-4}	6.186×10^{-3}	1.125×10^{-2}	1.799×10^{-2}	2.348×10^{-2}	2.902×10^{-2}
ReLu	[15, 15, 15, 15, 15]	1.041×10^{-3}	1.557×10^{-3}	5.816×10^{-3}	1.137×10^{-2}	1.676×10^{-2}	2.546×10^{-2}	2.803×10^{-2}

were extracted and stored, with 100 values selected for each parameter within their designated intervals.

The parameters for $C_f(Re_x)^{1/2}$ included $We \in [1, 2]$, $\phi \in [0.001, 0.008]$, $\alpha \in [0, 2\pi]$, $Ha \in [0, 1]$, $A \in [0, 1]$, and $M_0 \in [0.1, 0.5]$. Figure 6 compares six regression models based on the coefficient of determination (R^2) in Fig. 6(a), the MSE in Fig. 6(b), and their prediction performance in Fig. 9. The GPR model achieves the highest accuracy, with an R^2 score of 0.957 and the lowest MSE, followed closely by SVR and tree-based models, while traditional linear models perform moderately. Figure 7 presents the correlation matrices for the six regression models that predict $C_f(Re_x)^{1/2}$. *We* consistently shows the strongest positive correlation with the predicted output across all models, with values near 0.88 for the ridge, lasso, and linear models and slightly lower in the GPR, SVR, and tree models. The remaining input parameters, ϕ, α, *Ha*, *A*, and M_0, exhibit weaker and more model-dependent correlations. GPR and tree models revealed

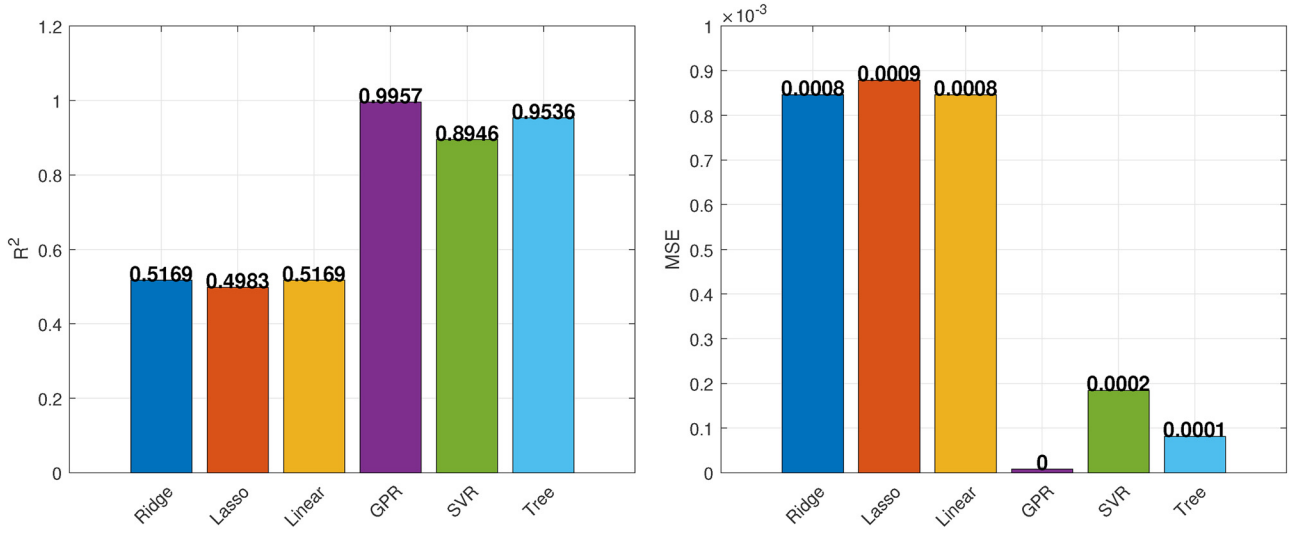

(a) Coefficient of determination (b) Mean squared error

FIG. 6. Coefficient of determination and mean squared error for linear and nonlinear regression models predicting the $C_f(Re_x)^{1/2}$.

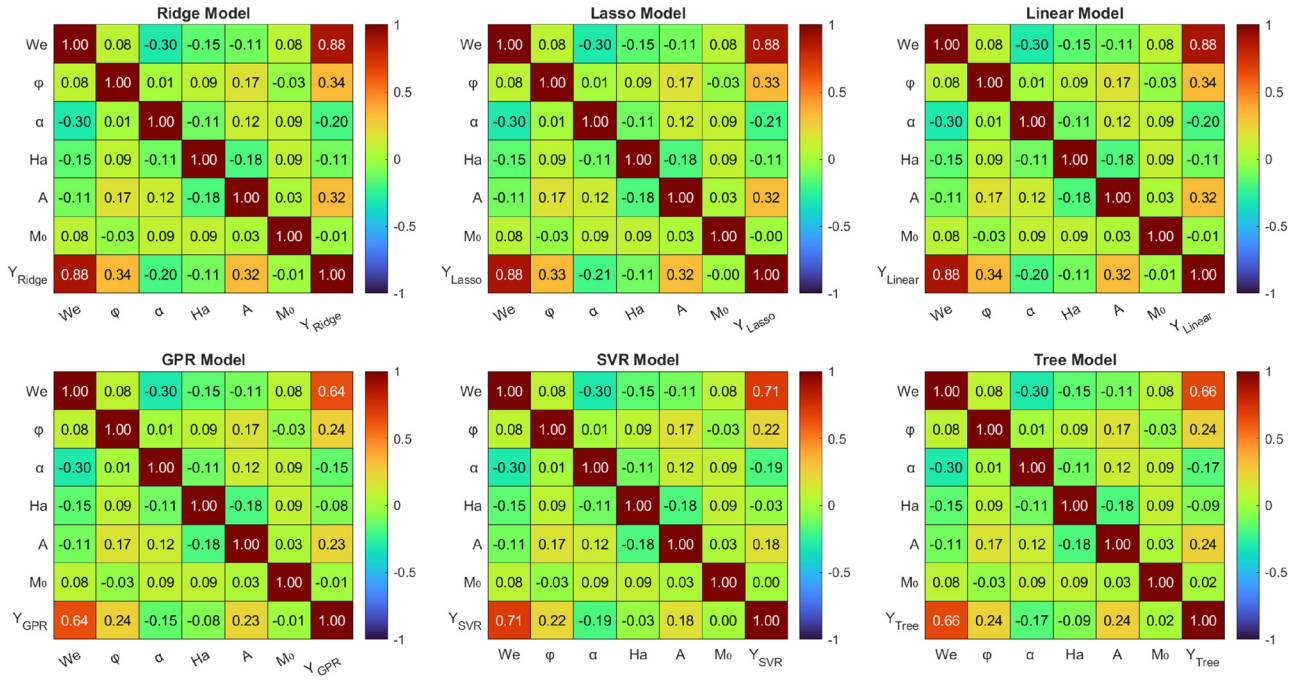

FIG. 7. Correlation matrix of the linear and nonlinear regression models for $C_f(Re_x)^{1/2}$.

more balanced correlations across multiple variables, indicating their ability to capture nonlinear interactions effectively. These results suggest that while *We* is the dominant predictor, nonlinear models offer better insight into the complex contributions of other variables. Figure 8 presents contour plots showing the interaction effects of selected parameter pairs on the local skin friction coefficient $C_f(Re_x)^{1/2}$. Figure 8(a) illustrates the influence of solid volume fraction ϕ (x axis) and magnetic field parameter M_0 (y axis), where increasing both leads to a gradual reduction in $C_f(Re_x)^{1/2}$. Figure 8(b) examines the combined effects of the stretching parameter A and the Weissenberg number *We*, revealing nonlinear behavior with distinct minima and maxima in the response surface. Figure 8(c) demonstrates that increasing M_0 (y axis) and *We* (x axis) together causes an almost linear decrease in the skin friction coefficient. Figure 9 further confirms that the GPR and SVR models closely track the actual data, validating the effectiveness of nonlinear regression methods in modeling nanofluid flow dynamics.

For the $Nu(Re_x)^{-\frac{1}{2}}$, the key parameters were varied as follows: $We \in [1,2]$, $\phi \in [0.001, 0.008]$, $\alpha \in [0, 2\pi]$, $Ha \in [0,1]$, $A \in [0,1]$, $M_0 \in [0.1, 0.5]$, $Ec \in [0,1]$, $s_1 \in [0.1, 0.5]$, and $Q \in [0.1, 0.5]$. The computed values of $Nu(Re_x)^{-\frac{1}{2}}$ were used to train and evaluate the regression models. Figure 10 summarizes model performance. Figure 10(a) shows that GPR attains the highest R^2 value of 0.9759, followed by the tree model with $R^2 = 0.9677$, while ridge, lasso, and linear models perform comparatively lower (around 0.867). In Fig. 10(b), the tree and GPR models achieve the lowest MSE values of 0.1465 and 0.1671, respectively. Figure 11 shows the correlation matrices of the six regression models that predict $Nu(Re_x)^{-1/2}$. In all the models, *We*, s_1, and Q^* show the most significant correlations with the predicted

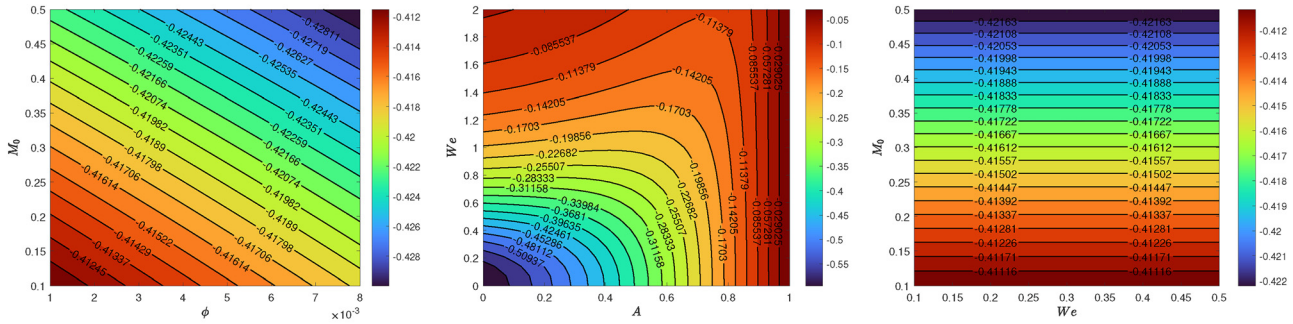

(a) Impact of ϕ and M_0 (b) Impact of A and *We* (c) Impact of M_0 and *We*

FIG. 8. Impact of various parameters on $C_f(Re_x)^{1/2}$.

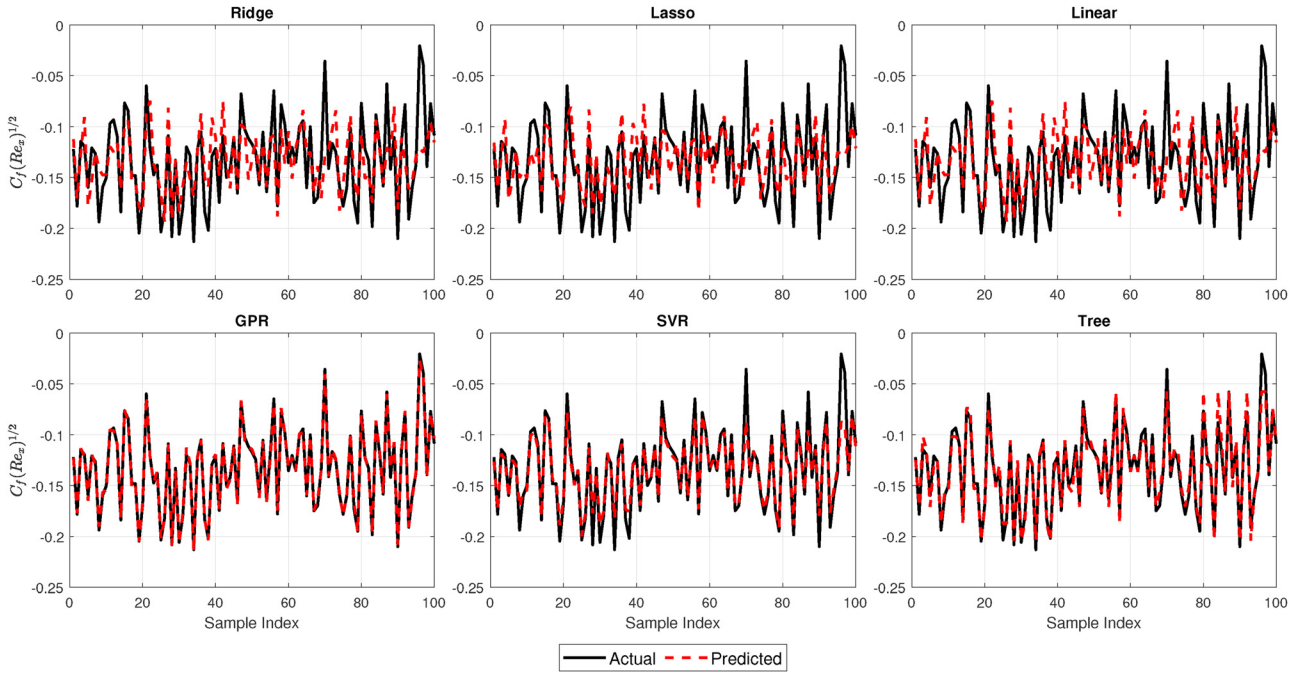

FIG. 9. Actual and prediction of $C_f(Re_x)^{1/2}$.

output. Q^* shows a clear negative correlation with $Nu(Re_x)^{-1/2}$ across all models, especially in the ridge, lasso, and linear models. *Ec* also shows a consistent negative effect in most models. Variables such as ϕ, *Ha*, and *A* have weaker and less consistent relationships. The GPR and SVR models capture these correlations slightly more strongly, possibly because of their ability to handle complex interactions. Figure 12 displays contour plots showing the combined influence of key parameter pairs on the local Nusselt number $Nu(Re_x)^{-1/2}$, which characterizes heat transfer behavior in the flow system. Figure 12(a) illustrates the interaction between the stretching parameter *A* and the first-order slip parameter s_1, where increased values of both variables enhance convective heat transfer, leading to a rise in $Nu(Re_x)^{-1/2}$. Figure 12(b) shows the effect of the Weissenberg number *We* and internal heat generation parameter Q^*; both reduce the Nusselt number, indicating that strong elastic and thermal source effects suppress surface heat transfer. In Fig. 12(b), the combination of the Eckert number *Ec* and the Hartmann number *Ha* leads to a monotonic decline in $Nu(Re_x)^{-1/2}$, highlighting the role of viscous heating and magnetic damping in

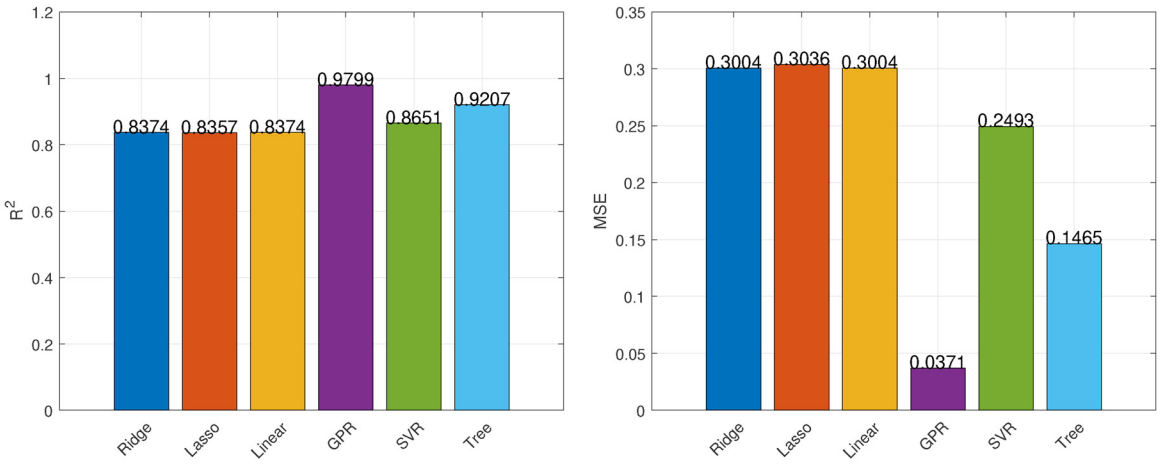

(a) Coefficient of determination (b) Mean squared error

FIG. 10. Coefficient of determination and mean squared error for linear and nonlinear regression models predicting the $Nu(Re_x)^{-\frac{1}{2}}$.

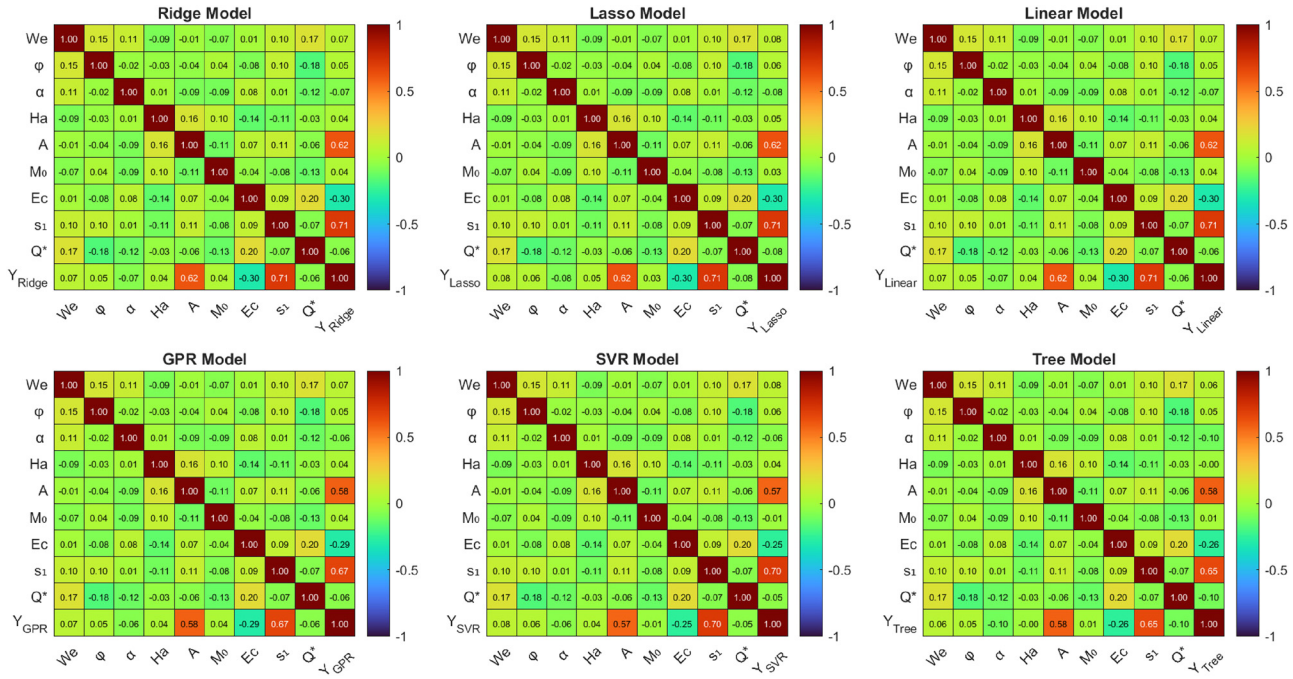

FIG. 11. Correlation matrix of the linear and nonlinear regression models for $Nu(Re_x)^{-\frac{1}{2}}$.

reducing thermal efficiency. Figure 13 reveals that GPR, SVR, and tree models accurately capture the target values, while linear models show greater deviation. These outcomes demonstrate the superiority of GPR and tree-based approaches in modeling heat transfer in nanofluid systems.

The $Sh(Re_x)^{-\frac{1}{2}}$ was modeled by varying $Sc \in [1, 2]$, $\phi \in [0.001, 0.008]$, $Kr \in [0.001, 0.008]$, $s_2 \in [0.1, 0.5]$, and $k'' \in [0.1, 0.5]$. Figure 14 presents model evaluation results. In Fig. 14(a), the GPR model achieves a perfect R^2 score of 1, outperforming other models, with ridge and linear regressions reaching 0.97. Figure 14(b) corroborates this with GPR recording zero MSE, while ridge, lasso, and linear regressions maintain low error around 0.0013. Figure 15 presents the correlation matrices for the six regression models predicting $Sh(Re_x)^{-1/2}$. In all models, the variables Sc and s_2 exhibit the strongest positive correlation with the output, suggesting that higher values of these parameters are associated with an increase in $Sh(Re_x)^{-1/2}$. Conversely, k'' consistently demonstrates a strong negative correlation across all models, indicating a reduction in the $Sh(Re_x)^{-1/2}$. The variables ϕ and Kr display a weak or nearly negligible correlation with the output. The consistency observed across models indicates that the relationship between these inputs and the output remains stable, irrespective of the model employed. Figure 16 explores parameter interactions. Figure 16(a) shows that increasing Kr and s_2 enhances $Sh(Re_x)^{-\frac{1}{2}}$, due to stronger chemical reactions and wall suction. Figure 16(b) displays a similar trend for Sc and Kr, while Fig. 16(c) highlights the synergistic effect of Sc and s_2

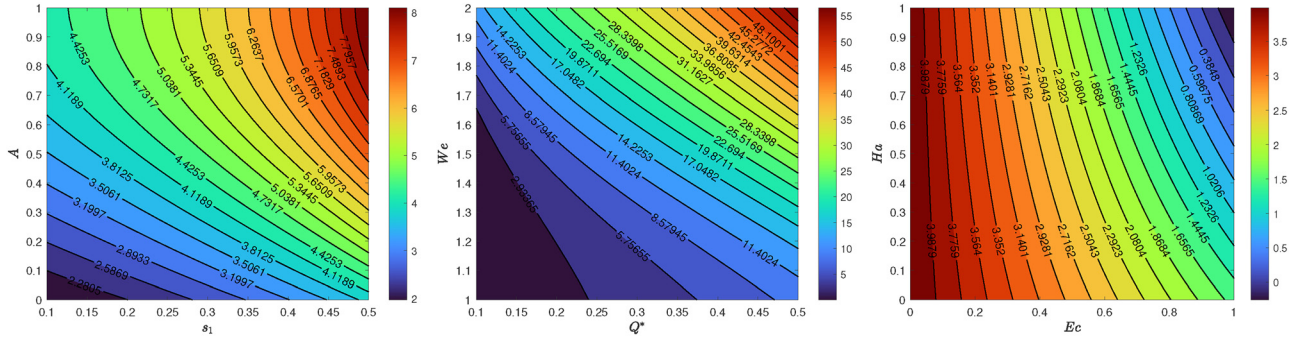

(a) Impact of A and s_1 (b) Impact of We and Q^* (c) Impact of Ec and Ha

FIG. 12. Impact of various parameters on $Nu(Re_x)^{-\frac{1}{2}}$.

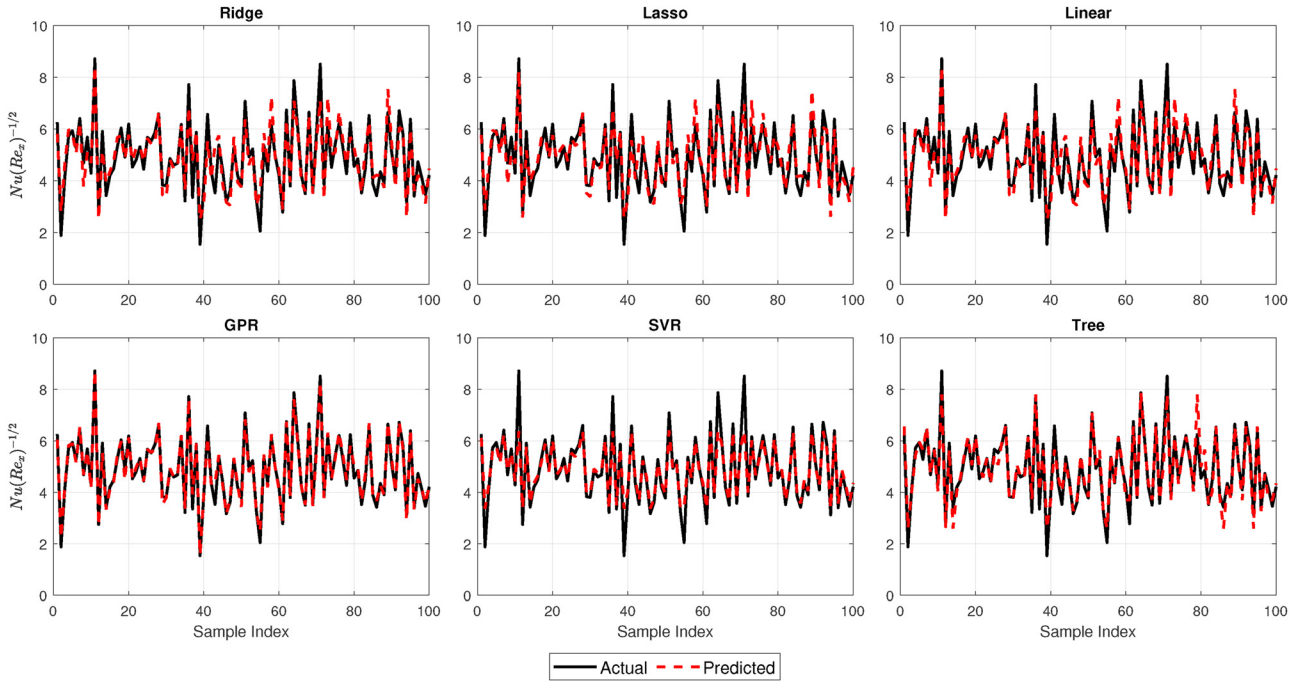

FIG. 13. Actual and prediction of $Nu(Re_x)^{-\frac{1}{2}}$.

on concentration boundary layer thinning. Finally, Fig. 17 visually confirms the strong predictive ability of GPR, with its predictions nearly identical to actual values. Ridge, lasso, and linear models also perform reliably, whereas SVR and tree regressions exhibit slight deviations. These findings affirm that GPR is the most effective model for predicting mass transfer characteristics in nanofluid systems.

V. CONCLUSION

In this study, the two-dimensional flow of a Carreau nanofluid over a thin stretching surface was examined by incorporating melting heat effects and considering both thermal and concentration stratification under an inclined magnetic field with multiple slip conditions. Milk served as the base fluid, and MgO nanoparticles were introduced to address magnesium deficiency in various applications. A data-driven

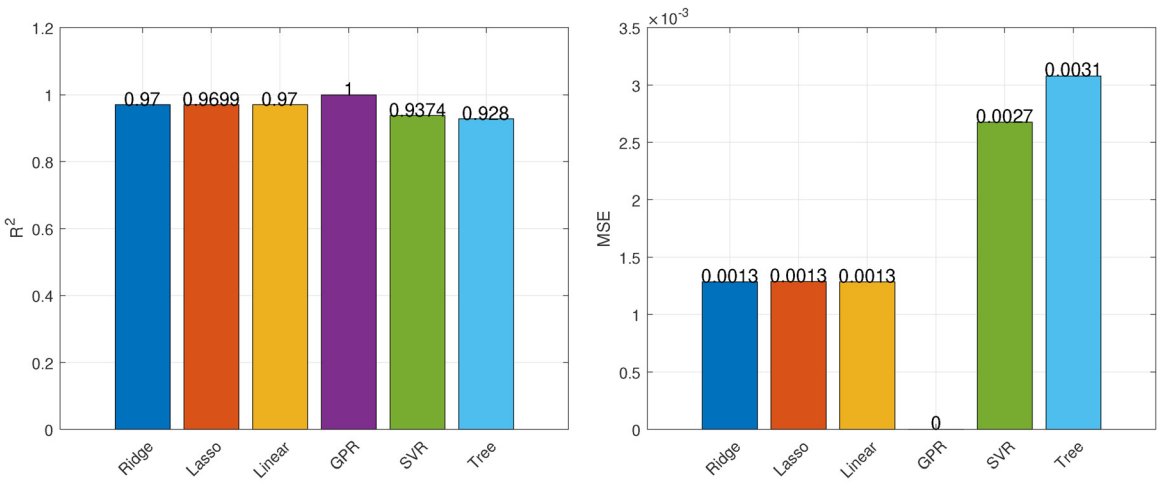

(a) Coefficient of determination (b) Mean squared error

FIG. 14. Coefficient of determination and mean squared error for linear and nonlinear regression models predicting the $Sh(Re_x)^{-\frac{1}{2}}$.

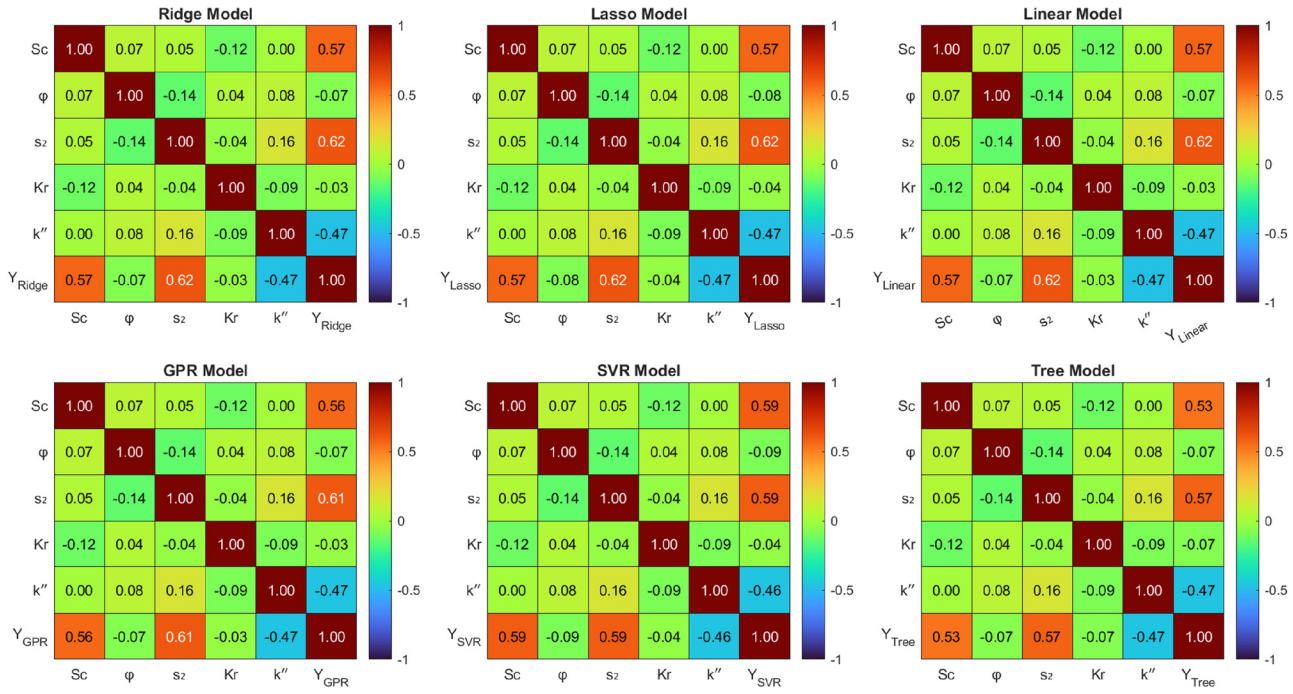

FIG. 15. Correlation matrix of the linear and nonlinear regression models for $Sh(Re_x)^{-\frac{1}{2}}$.

approach utilizing a BR-BPNN was employed to verify the accuracy and reliability of the computed velocity, temperature, and concentration profiles. To evaluate the robustness of the model, Gaussian noise of varying intensities was introduced, and the neural network was trained on both noise-free and noisy datasets. Model performance was assessed using the relative error computed via the Euclidean norm, with results supported by comparative plots and error graphs. Additionally, key engineering quantities were estimated using various linear and nonlinear regression models, with the GPR model demonstrating perfect agreement with the exact evaluations. The findings indicated that the proposed regression-based data-driven framework yields accurate and stable solutions, even in input uncertainty and data noise.

The findings of this study had potential applications in areas such as cancer treatment, tissue engineering, drug delivery, cryopreservation, antimicrobial therapy, bone regeneration, and bio-sensing. It was observed that an increase in the melting parameter enhanced the velocity due to intensified convective transport toward the cooling surface, while the temperature exhibited an inverse relationship with the melting parameter. Additionally, a higher *We* led to a reduction in velocity, attributed to the dominance of elastic forces that increased the fluid's resistance to flow. Furthermore, the temperature profile increased with a rise in the *Ec* as a consequence of enhanced viscous dissipation and internal heat generation.

This study highlights the effectiveness of combining numerical schemes with regression-based data-driven approaches to examine

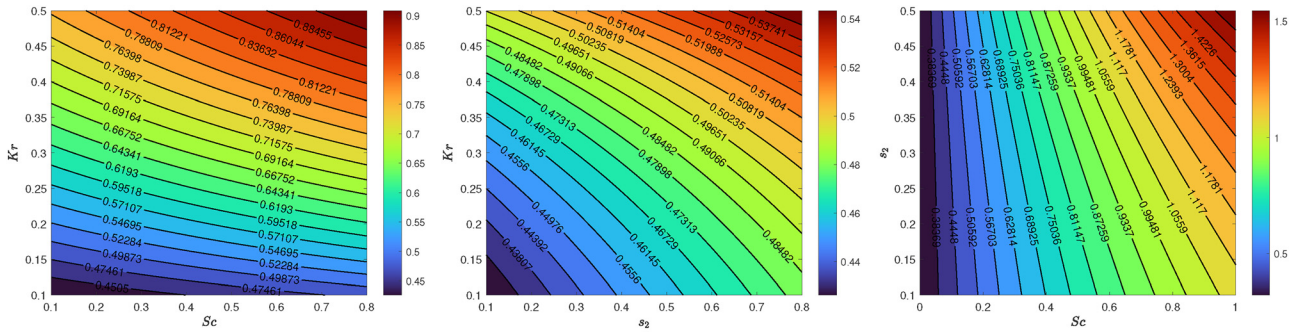

(a) Impact of Kr and s_2 (b) Impact of Sc and Kr (c) Impact of Sc and s_2

FIG. 16. Impact of various parameters on $Sh(Re_x)^{-\frac{1}{2}}$.

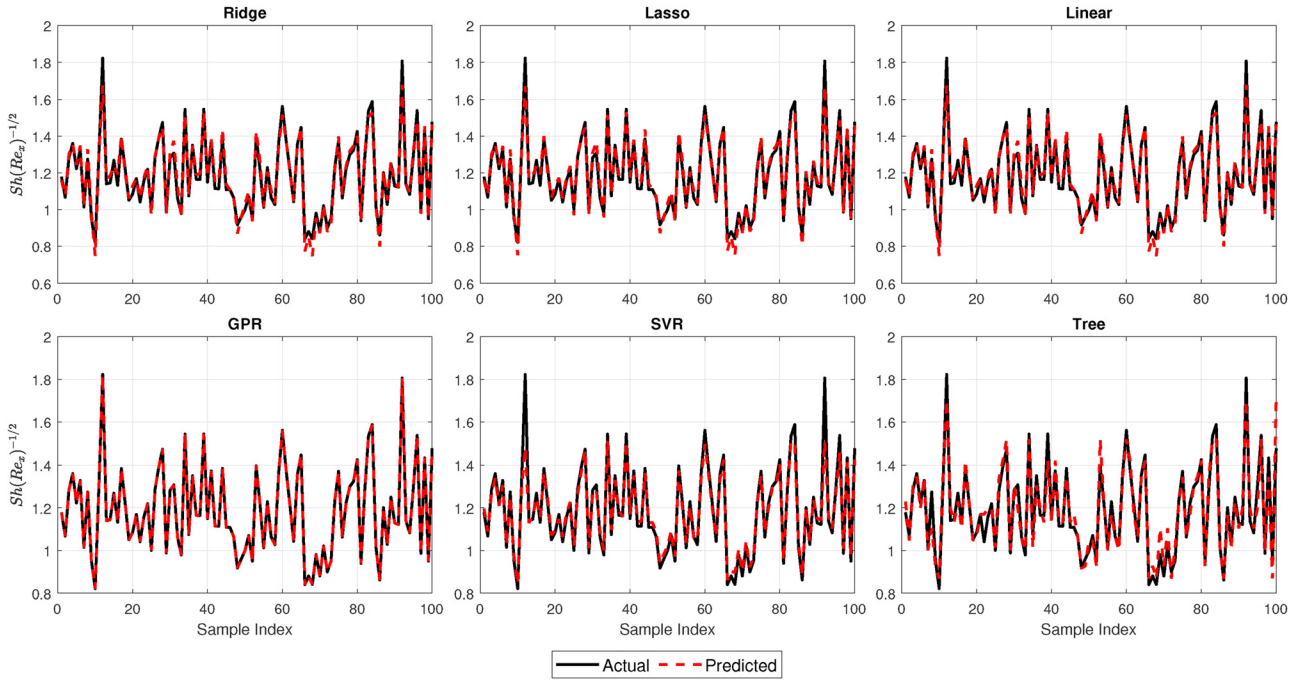

FIG. 17. Actual and prediction of $Sh(Re_x)^{-\frac{1}{2}}$.

highly nonlinear thermal systems. In future work, we aim to apply two distinct methodologies: one based on physics-informed neural networks and the other involving a bio-inspired algorithm integrated with active search strategies to directly solve highly nonlinear thermal systems of equations with enhanced accuracy and efficiency.

ACKNOWLEDGMENTS

Aamir Farooq acknowledges the postdoctoral fellowship supported by Zhejiang Normal University, China, under Grant No. YS304024913. Wen Xiu Ma acknowledges support from the Ministry of Science and Technology of China (Nos. G2021016032L and G2023016011L) and the National Natural Science Foundation of China (NSFC) under Grant Nos. 12271488 and 11975145.

AUTHOR DECLARATIONS

Conflict of Interest

The authors have no conflicts to disclose.

Author Contributions

Aamir Farooq: Conceptualization (equal); Data curation (equal); Formal analysis (equal); Software (equal); Writing – original draft (equal). **Sadique Rehman:** Formal analysis (equal); Writing – review & editing (equal). **Wen-Xiu Ma:** Supervision (equal); Writing – review & editing (equal).

DATA AVAILABILITY

The data that support the findings of this study are available within the article.

REFERENCES

[1]O. A. Abo-zaid, R. A. Mohamed, F. M. Hady, and A. Mahdy, "MHD Powell–Eyring dusty nanofluid flow due to stretching surface with heat flux boundary condition," J. Egypt. Math. Soc. **29**(1), 14 (2021).
[2]M. W. Ahmad, J. Reynolds, and Y. Rezgui, "Predictive modelling for solar thermal energy systems: A comparison of support vector regression, random forest, extra trees and regression trees," J. Cleaner Prod. **203**, 810–821 (2018).
[3]F. Ali and N. Summayya, "Numerical simulation of Cattaneo–Christov double-diffusion theory with thermal radiation on MHD Eyring–Powell nanofluid towards a stagnation point," Int. J. Ambient Energy **43**(1), 4939–4949 (2021).
[4]J. Azarnoosh and F. Hassanipour, "Fluid-structure interaction modeling of lactating breast: Newtonian vs. non-Newtonian milk," J. Biomech. **124**, 110500 (2021).
[5]S. A. Bagherzadeh, A. H. M. Isfahani, I. K. Asfeh, and M. Nouri, "A Bayesian regularization back propagation (BRBP) neural network model for prediction of the effect of using Al_2O_3–Fe_2O_3 hybrid nano fuels on the performance and emissions of diesel engines," Clean Technol. Environ. Policy (published online 2025).
[6]I. Benemerito, F. Ewbank, A. Narracott, M.-C. Villa-Uriol, A. P. Narata, U. Patel, D. Bulters, and A. Marzo, "Computational fluid dynamics and shape analysis enhance aneurysm rupture risk stratification," Int. J. Comput. Assisted Radiol. Surg. **20**, 31–41 (2024).
[7]M. Bilal and S. Ashbar, "Flow and heat transfer analysis of Eyring-Powell fluid over stratified sheet with mixed convection," J. Egypt. Math. Soc. **28**(1), 40 (2020).
[8]S. Bransburg-Zabary, A. Virozub, and F. B. Mimouni, "Human milk warming temperatures using a simulation of currently available storage and warming methods," PLoS One **10**(6), e0128806 (2015).
[9]F. Burden and D. Winkler, "Bayesian regularization of neural networks," *Artificial Neural Networks: Methods Applications* (Springer, 2009), pp. 23–42.
[10]A. Carlucci, D. Petronio, D. Barsi, M. Dellacasagrande, and D. Simoni, "Tuning of an algebraic model for separated flows by means of Bayesian Lasso," in *ASME Turbo Expo: Turbomachinery Technical Conference and Exposition* (American Society of Mechanical Engineers, 2024).

[11]A. J. Chamkha and I. Pop, "Effect of thermophoresis particle deposition in free convection boundary layer from a vertical flat plate embedded in a porous medium," Int. Commun. Heat Mass Transfer **31**(3), 421–430 (2004).
[12]A. Darvesh, F. M. Maiz, B. Souayeh, M. Sánchez-Chero, H. A. Garalleh, L. J. C. Santisteban, and C. N. P. Leonardo, "Advanced ANN computational procedure for thermal transport prediction in polymer-based ternary radiative Carreau nanofluid with extreme shear rates over bullet surface," Appl. Rheol. **35**(1), 20240029 (2025).
[13]Y. Duan, C. Cooling, J. S. Ahn, C. Jackson, A. Flint, M. D. Eaton, and M. J. Bluck, "Using a Gaussian process regression inspired method to measure agreement between the experiment and CFD simulations," Int. J. Heat Fluid Flow **80**, 108497 (2019).
[14]A. Farooq, S. Rehman, A. N. Alharbi, M. Kamran, T. Botmart, and I. Khan, "Closed-form solution of oscillating maxwell nano-fluid with heat and mass transfer," Sci. Rep. **12**(1), 12205 (2022).
[15]K. Gangadhar, M. A. Kumari, and A. J. Chamkha, "EMHD flow of radiative second-grade nanofluid over a Riga plate due to convective heating: Revised Buongiorno's nanofluid model," Arab. J. Sci. Eng. **47**(7), 8093–8103 (2022).
[16]D. Gopal, S. Naik, N. Kishan, and C. S. K. Raju, "The impact of thermal stratification and heat generation/absorption on MHD Carreau nano fluid flow over a permeable cylinder," SN Appl. Sci. **2**(4), 639 (2020).
[17]S. Rama, G. Reddy, C. Ali, and A. M. Rashad, "Mixed convective boundary layer flow over a vertical wedge embedded in a porous medium saturated with a nanofluid," in *3rd International Conference on Thermal Issues in Emerging Technologies Theory and Applications* (IEEE, 2010), pp. 445–451.
[18]S. K. Gupta, K. Sambyo, and S. Shekhar, "Extra tree regressor and Tree-structured Parzen estimator based machine learning model for predicting nanofluid's Nusselt number," Eng. Res. Express **7**, 015284 (2025).
[19]M. T. Hagan, H. B. Demuth, and M. Beale, *Neural Network Design* (PWS Publishing Co., 1997).
[20]M. M. Hasan, M. M. Rahman, S. Abu Bakar, M. N. Kabir, D. Ramasamy, and A. H. M. Saifullah Sadi, "Performance evaluation of various training functions using ANN to predict the thermal conductivity of EG/water-based GNP/CNC hybrid nanofluid for heat transfer application," J. Therm. Anal. Calorim. **150**, 1907–1926 (2025).
[21]J. Iqbal, Y. Akbar, and M. M. Alam, "Bayesian regularization-based intelligent computing for peristaltic propulsion of curvature-dependent channel walls," Phys. Fluids **37**(2), 023101 (2025).
[22]M. Irfan, M. Khan, and W. A. Khan, "Behavior of stratifications and convective phenomena in mixed convection flow of 3D Carreau nanofluid with radiative heat flux," J. Braz. Soc. Mech. Sci. Eng. **40**(11), 521 (2018).
[23]M. Javed and M. Farooq, "Mixed convection and melting rheology in dual stratified Eyring-Powell nanofluid flow over surface of variable thickness: Buongiorno model approach," Int. Commun. Heat Mass Transfer **125**, 105322 (2021).
[24]M. Kayri, "Predictive abilities of Bayesian regularization and Levenberg–Marquardt algorithms in artificial neural networks: A comparative empirical study on social data," Math. Comput. Appl. **21**(2), 20 (2016).
[25]M. Khan, T. Salahuddin, and M. Y. Malik, "An immediate change in viscosity of Carreau nanofluid due to double stratified medium: Application of Fourier's and Fick's laws," J. Braz. Soc. Mech. Sci. Eng. **40**(9), 457 (2018).
[26]N. Safwa Khashi'ie, N. M. Arifin, M. M. Rashidi, E. Hafidz Hafidzuddin, and N. Wahi, "Magnetohydrodynamics (MHD) stagnation point flow past a shrinking/stretching surface with double stratification effect in a porous medium," J. Therm. Anal. Calorim. **139**(6), 3635–3648 (2020).
[27]J. Kierzenka and L. F. Shampine, "A BVP solver based on residual control and the Maltab PSE," ACM Trans. Math. Software **27**(3), 299–316 (2001).
[28]M. Veera Krishna, N. Ameer Ahamad, and A. J. Chamkha, "Hall and ion slip impacts on unsteady MHD convective rotating flow of heat generating/absorbing second grade fluid," Alexandria Eng. J. **60**(1), 845–858 (2021).
[29]M. Veera Krishna, P. V. S. Anand, and A. J. Chamkha, "Heat and mass transfer on free convective flow of amicropolar fluid through a porous surface with inclined magnetic field and Hall effects," Spec. Top. Rev. Porous Media **10**(3), 203 (2019).
[30]B. Kumar, Prachi, A. Singhal, R. Nandkeolyar, P. Kumar, and A. J. Chamkha, "Regression analysis and features of negative activation energy for MHD nanofluid flow model: A comparative study," Propul. Power Res. **12**(2), 273–283 (2023).
[31]R. Kumar, S. A. Shehzad, and A. J. Chamkha, "Optimal treatment of stratified Carreau and Casson nanofluids flows in Darcy-Forchheimer porous space over porous matrix," Appl. Math. Mech. **41**(11), 1651–1670 (2020).
[32]B. Kumbhakar and S. Nandi, "Unsteady MHD radiative-dissipative flow of Cu-Al_2O_3/H_2O hybrid nanofluid past a stretching sheet with slip and convective conditions: A regression analysis," Math. Comput. Simul. **194**, 563–587 (2022).
[33]B. Kumbhakar, S. Nandi, and A. J. Chamkha, "Unsteady hybrid nanofluid flow over a convectively heated cylinder with inclined magnetic field and viscous dissipation: A multiple regression analysis," Chin. J. Phys. **79**, 38–56 (2022).
[34]D. J. C. MacKay, "A practical Bayesian framework for backpropagation networks," Neural Comput. **4**(3), 448–472 (1992).
[35]A. Mahdy, "Unsteady mixed bioconvection flow of Eyring–Powell nanofluid with motile gyrotactic microorganisms past stretching surface," BioNanoSci. **11**(2), 295–305 (2021).
[36]D. Mohanty, G. Mahanta, and S. Shaw, "Irreversibility and thermal performance of nonlinear radiative cross-ternary hybrid nanofluid flow about a stretching cylinder with industrial applications," Powder Technol. **433**, 119255 (2024).
[37]D. Mohanty, G. Mahanta, S. Shaw, and R. Katta, "Entropy and thermal performance on shape-based 3D tri-hybrid nanofluid flow due to a rotating disk with statistical analysis," J. Therm. Anal. Calorim. **149**, 12285–12306 (2024).
[38]H. A. Nabwey, S. I. Alshber, A. M. Rashad, and A. E. N. Mahdy, "Influence of bioconvection and chemical reaction on magneto—Carreau nanofluid flow through an inclined cylinder," Mathematics **10**(3), 504 (2022).
[39]R. Naz, S. Tariq, M. Sohail, and Z. Shah, "Investigation of entropy generation in stratified MHD Carreau nanofluid with gyrotactic microorganisms under Von Neumann similarity transformations," Eur. Phys. J. Plus **135**(2), 178 (2020).
[40]M. Nielen, H. Deluyker, Y. H. Schukken, and A. Brand, "Electrical conductivity of milk: Measurement, modifiers, and meta analysis of mastitis detection performance," J. Dairy Sci. **75**(2), 606–614 (1992).
[41]C. Parida, M. V. Lekgari, G. Mahanta, and S. Shaw, "Multi-layer neural network on 3D transition metal hydrides-based ternary nanofluid flow with entropy: Application to spinning disc reactor," Therm. Sci. Eng. Prog. **62**, 103641 (2025).
[42]C. S. K. Raju, N. A. Ahammad, K. Sajjan, N. A. Shah, S.-J. Yook, and M. D. Kumar, "Nonlinear movements of axisymmetric ternary hybrid nanofluids in a thermally radiated expanding or contracting permeable Darcy Walls with different shapes and densities: Simple linear regression," Int. Commun. Heat Mass Transfer **135**, 106110 (2022).
[43]M. Ramzan, S. Rehman, M. S. Junaid, A. Saeed, P. Kumam, and W. Watthayu, "Dynamics of Williamson ferro-nanofluid due to bioconvection in the portfolio of magnetic dipole and activation energy over a stretching sheet," Int. Commun. Heat Mass Transfer **137**, 106245 (2022).
[44]P. Rana, X. Zhu, and I. Pop, "Multiplicity and stability of solutions in transport phenomena of non-Newtonian Carreau nanofluid with nonlinear Rosseland thermal approximations and neural prediction," Case Stud. Therm. Eng. **68**, 105821 (2025).
[45]S. Rehman, A. Anjum, M. Farooq, M. Y. Malik *et al.*, "Melting heat phenomenon in thermally stratified fluid reservoirs (Powell-Eyring fluid) with joule heating," Int. Commun. Heat Mass Transfer **137**, 106196 (2022).
[46]Z. Sabir, S. Khansa, G. Baltaji, and T. Saeed, "A Bayesian regularization neural network procedure to solve the language learning system," Knowl.-Based Syst. **310**, 112997 (2025).
[47]A. Sahoo and R. Nandkeolyar, "Entropy generation in convective radiative flow of a Casson nanofluid in non-darcy porous medium with hall current and activation energy: The multiple regression model," Appl. Math. Comput. **402**, 125923 (2021).
[48]S. K. Sahu, S. Rout, S. Shaw, N. Dash, D. N. Thatoi, and M. K. Nayak, "Hydrothermal stagnation point flow of Carreau nanofluid over a moving thin needle with non-linear Navier's slip and cubic autocatalytic chemical reactions in Darcy-Forchheimer medium," J. Indian Chem. Soc. **99**(11), 100741 (2022).
[49]M. Saleem, A. H. Majeed, I. Ahmad, and A. R. Ali, "Symmetry-based analysis of nonlinear mixed convection in 3D EMHD nano-Carreau fluid flow with Riga stretched surface effects and multi-physical interactions," J. Appl. Math. Mech./Z. Angew. Math. Mech. **104**(9), e202400072 (2024).

[50]R. D. Sanhueza, I. Akkerman, and J. W. R. Peeters, "Machine learning for the prediction of the local skin friction factors and Nusselt numbers in turbulent flows past rough surfaces," Int. J. Heat Fluid Flow **103**, 109204 (2023).
[51]S. J. K. Sasidharan, N. Parasumanna Krishnamurthy, R. Mamat, V. D. Loganathan, and R. Sathyamurthy, "Synthesis, characterisation and thermo-physical investigations on magnesia nanoparticles dispersed in ethylene glycol–DI water (50:50)," Micro Nano Lett. **13**(3), 335–340 (2018).
[52]S. S. S. Sen, R. Mahato, S. Shaw, and M. Das, "Simulation of entropy and heat and mass transfer in water-EG based hybrid nanoliquid flow with MHD and nonlinear radiation," Numer. Heat Transfer, Part A **85**(19), 3253–3267 (2024).
[53]L. F. Shampine, J. Kierzenka, M. W. Reichelt *et al.*, "Solving boundary value problems for ordinary differential equations in MATLAB with bvp4c," Tutorial Notes **2000**, 1–27.
[54]M. Sorgun, A. Murat Ozbayoglu, and M. Evren Ozbayoglu, "Support vector regression and computational fluid dynamics modeling of Newtonian and non-Newtonian fluids in annulus with pipe rotation," J. Energy Res. Technol. **137**(3), 032901 (2015).
[55]K. Tyagi, C. Rane, M. Manry *et al.*, "Regression analysis," in *Artificial Intelligence and Machine Learning for EDGE Computing* (Elsevier, 2022), pp. 53–63.
[56]F. Wang, S. Rehman, J. Bouslimi, H. Khaliq, M. I. Qureshi, M. Kamran, A. N. Alharbi, H. Ahmad, and A. Farooq, "Comparative study of heat and mass transfer of generalized MHD Oldroyd-B bio-nano fluid in a permeable medium with ramped conditions," Sci. Rep. **11**(1), 23454 (2021).
[57]H. Waqas, U. Farooq, M. S. Alqarni, and T. Muhammad, "Numerical investigation for 3D bioconvection flow of Carreau nanofluid with heat source/sink and motile microorganisms," Alexandria Eng. J. **61**(3), 2366–2375 (2022).
[58]W.-F. Xia, F. Haq, M. Saleem, M. Ijaz Khan, S. U. Khan, and Y.-M. Chu, "Irreversibility analysis in natural bio-convective flow of Eyring-Powell nanofluid subject to activation energy and gyrotactic microorganisms," Ain Shams Eng. J. **12**(4), 4063–4074 (2021).
[59]I. Zari, A. Shafiq, G. Rasool, T. N. Sindhu, and T. S. Khan, "Double-stratified Marangoni boundary layer flow of Casson nanoliquid: Probable error application," J. Therm. Anal. Calorim. **147**(12), 6913–6929 (2022).